1   **ATR kinase inhibition induces thymineless death in proliferating CD8+ T cells**

2

3   Norie Sugitani[1], Frank P. Vendetti[1], Andrew J. Cipriano[1], Joshua J. Deppas[2], Tatiana N. Moiseeva[3],

4   Sandra Schamus-Haynes[1], Yiyang Wang[4], Drake Palmer[5], Hatice U. Osmanbeyoglu[6], Anna

5   Bostwick[7], Nathaniel W. Snyder[7], Yi-Nan Gong[4], Katherine M. Aird[8], Greg M. Delgoffe[4], Jan H.

6   Beumer[2, 9], and Christopher J. Bakkenist[1,8]

7

8   [1]Department of Radiation Oncology, UPMC Hillman Cancer Center, School of Medicine,

9   University of Pittsburgh, Pittsburgh, Pennsylvania, PA

10   [2]Department of Pharmaceutical Sciences, School of Pharmacy, University of Pittsburgh,

11   Pittsburgh, PA

12   [3]Tallinn University of Technology, Department of Chemistry and Biotechnology, Tallinn, Estonia

13   [4]Department of Immunology, UPMC Hillman Cancer Center, School of Medicine, University of

14   Pittsburgh, Pittsburgh, Pennsylvania, PA

15   [5]UPMC Hillman Cancer Center, Department of Medicine, University of Pittsburgh School of

16   Medicine, Pittsburgh, PA

17   [6]Department of Biomedical Informatics, UPMC Hillman Cancer Center, School of Medicine,

18   University of Pittsburgh, Pittsburgh, Pennsylvania, PA

19   [7]Lewis Katz School of Medicine at Temple University, Center for Metabolic Disease Research,

20   Department of Cardiovascular Sciences, Philadelphia, PA USA

21   [8]Department of Pharmacology and Chemical Biology, UPMC Hillman Cancer Center, School of

22   Medicine, University of Pittsburgh, Pittsburgh, Pennsylvania, PA

23   [9]Division of Hematology-Oncology, UPMC Hillman Cancer Center, Department of Medicine,

24   University of Pittsburgh School of Medicine, Pittsburgh, PA

25

26 **SUMMARY**

27 **ATR kinase is a central regulator of the DNA damage response (DDR) and cell cycle checkpoints.**

28 **However, little is known about the role of ATR in the cell cycle and the impact of DDR inhibitors**

29 **in immune cells in the absence of DNA damage. We previously showed that the ATR inhibitor**

30 **AZD6738 (ATRi) combines with radiation to generate delayed, CD8+ T cell-dependent antitumor**

31 **responses in mouse models of cancer. Here, we show that ATRi induces untimely CDK1 activity**

32 **during S phase in CD8+ T cells and this induces origin firing and simultaneous degradation of**

33 **dNTP synthesis and salvage enzymes. These pleiotropic effects of ATRi in proliferating CD8+ T**

34 **cells induce deoxyuridine contamination in genomic DNA, R loops, RNA-DNA polymerase**

35 **collisions, and death. Remarkably, thymidine significantly rescues ATRi-induced CD8+ T cell**

36 **death. Our data identifies critical considerations for the design of clinical ATRi regimens with**

37 **genotoxic chemo- and radiation and immunotherapies.**

38

39 **KEYWORDS**

40 ATR/CD8+ T cells/origin firing/deoxyuridine contamination/thymineless death

41

INTRODUCTION

Most chemotherapies target DNA replication forks and their efficacy is associated with both the direct killing of proliferating tumor cells and, in many cases, the stimulation of innate and adaptive anti-tumor immune responses (Bracci et al., 2014; O'Connor, 2015). One mechanism through which DNA damaging chemotherapies increase anti-tumor immune responses is the direct killing of proliferating immune cells causing transient leukocytopenia followed by a rebound proliferation of immune cell populations. A major clinical goal is to identify novel regimens that maximize the direct killing of tumor cells, while concurrently selecting for and stimulating the activity of anti-tumor immune effector cells.

The DNA Damage Response (DDR) is a signaling system that integrates nucleic acid metabolism and DNA repair with the cell cycle to safeguard genome stability (Ciccia and Elledge, 2010). DDR inhibitors (DDRi) have been developed to target tumors that have acquired inactivating mutations in a DNA repair pathway and to potentiate direct tumor cell killing by DNA damaging chemotherapies and radiotherapy. For example, Olaparib (Lynparza), the poly (ADP-ribose) polymerase (PARP) inhibitor, is approved for the treatment of tumors harboring BRCA1 or BRCA2 mutations. More recently, four ATR kinase inhibitors (we use the abbreviation ATRi's for these four inhibitors) have advanced to phase 1 and phase 2 trials: ceralasertib (AZD6738); berzosertib (M6620, VX-970); elimusertib (BAY 1895344); and RP-3500 (Foote et al., 2018; Hall et al., 2014; Roulston et al., 2021; Wengner et al., 2020). ATRi's potentiate chemotherapies that target DNA replication forks, selectively kill tumor cells with inactivating mutations in ATM, ERCC1, RNASE H2, and XRCC1, and block the upregulation of PD-L1 after radiation (Hustedt et al., 2019; Mohni et al., 2015; Roulston *et al.*, 2021; Sato et al., 2017; Vendetti et al., 2018; Vendetti et al., 2015; Wang et al., 2019). Phase I clinical trial data show that ATRi's suppress circulating monocytes and proliferating T cells, and that these populations rebound after cessation of ATRi's, as expected (Krebs et al., 2018). However, ATR inhibitor AZD6738 (we use the abbreviation ATRi for AZD6738) unexpectedly combines with radiation to generate delayed, CD8^{+} T cell-dependent responses in mouse models of cancer (Vendetti *et al.*, 2018). These preclinical and clinical findings suggest that the direct impact of ATRi in immune cells is clinically important and warrants further investigation.

70 ATR is an essential kinase that is activated at regions of single-stranded DNA that are generally

71 associated with stalled and collapsed DNA replication forks and resected DNA double strand

72 breaks (Brown and Baltimore, 2000; Cortez et al., 2001; Zou and Elledge, 2003). ATR kinase

73 phosphorylates and activates a second essential kinase, CHK1, that phosphorylates the CDC25A

74 phosphatase causing its degradation in the proteasome after DNA damage (Liu et al., 2000;

75 Mailand et al., 2000; Sanchez et al., 1997). Since CDC25A removes inhibitory phosphorylations

76 on the cyclin-dependent kinases CDK2 and CDK1 facilitating the G1/S and G2/M transitions,

77 respectively, CDC25A degradation induces cell cycle arrest (Hoffmann et al., 1994). While the role

78 of CDC25A degradation in cell cycle arrest after DNA damage is well-accepted, CDC25A is a

79 dynamic protein and the ATR-CHK1-CDC25A signaling axis has also been implicated in progression

80 though S phase in unperturbed cells (Sorensen et al., 2004). Whether ATR-CHK1-CDC25A

81 signaling limits origin firing through S phase to prevent replication fork stalling or repairs

82 replication forks stalled at endogenous DNA lesions or following mechanical failure in

83 unperturbed cells is not known.

84 ATRi induce origin firing across active replicons in human cancer cells and fibroblasts (Couch et

85 al., 2013; Kwok et al., 2016; Moiseeva et al., 2017; Moiseeva et al., 2019b). However, the

86 physiological and clinical significance of this signaling mechanism has not been established.

87 Computational models of the spatiotemporal pattern of origin firing point to an unknown

88 mechanism that limits additional origin firing within ~7–120 kb of an origin that fires (Lob et al.,

89 2016). Since the ~50,000 origins that replicate the human genome are generated from an excess

90 of ~500,000 licensed origins, we hypothesized that the first origin firing event within a replicon

91 may be stochastic and that ATR-CHK1-CDC25A signaling may then limit additional origin firing

92 across active replicons generating dormant or flexible origins that are passively replicated

93 (Mahbubani et al., 1997; Sorensen *et al.*, 2004). We further hypothesized that, through limiting

94 origin firing across active replicons, ATR-CHK1-CDC25A signaling may accommodate the supply

95 of dNTPs which is 50-fold less than that required to synthesize the genome in a human epithelial

96 cell (Ferraro et al., 2010).

97 To test these hypotheses in a clinically important model, we interrogated the impact of ATRi in

98 CD8^{+} T cells *ex vivo*. We show that ATRi induces deoxyuridine (dU) contamination in genomic

99   DNA, R loops, RNA-DNA polymerase collisions, and death in proliferating, but not naïve CD8+ T

100   cells. Remarkably, we show that thymidine significantly rescues ATRi-induced CD8+ T cell death.

101   Our results have far-reaching implications for the design of clinical trials combining ATRi with

102   immunotherapies and/or antimetabolites and suggest that dose limiting toxicity in active clinical

103   trials of ATRi may be associated with leukocytopenia caused by thymineless cell death.

104   **RESULTS**

105   **ATR kinase is essential in proliferating CD8+ T cells *ex vivo***

106   To study the impact of ATRi on the activation, proliferation, and survival of CD8+ T cells, we used

107   *ex vivo* activated CD8+ T cells derived from spleens and lymph nodes of C57BL/6 and Pmel-1 mice.

108   We used Pmel-1 CD8+ T cells activated with the synthetic peptide gp100 in splenocytes when the

109   experimental endpoint allowed the identification of CD8+ T cells. We used CD8+ T cells activated

110   with CD3Ɛ and CD28 antibodies after purification by negative selection when contaminating cells

111   could compromise the experimental endpoint.

112   To confirm the kinetics of activation and proliferation of CD8+ T cells *ex vivo*, we used a flow

113   cytometry assay of cell trace violet (CTV) dye dilution. CD8+ T cells were fully activated (CD44hi)

114   at ~21 h and started dividing at ~24 h (Figure 1A). Once activated, CD8+ T cells divided 4-5 times

115   from 24-48 h, consistent with a previous report (Yoon et al., 2010). To determine whether the

116   activation of CD8+ T cells was associated with increased expression of DDR and replication

117   proteins, we generated whole cell extracts from CD8+ T cells at 0 h and 30 h. Empirically we found

118   that ATM could be used to normalize the naïve and proliferating CD8+ T cells proteomes (Figure

119   1B). ATR and deoxycytidine kinase (DCK) were expressed in naïve CD8+ T cells and induced

120   significantly in proliferating CD8+ T cells. CHK1, the ribonucleotide reductase subunits RRM1 and

121   RRM2, deoxyuridine 5'-triphosphate nucleotidohydrolase (DUT), and WEE1 were expressed at

122   the limits of detection in naïve CD8+ T cells and highly expressed in proliferating CD8+ T cells.

123   To determine whether ATR kinase activity is required for the activation and proliferation of CD8+

124   T cells, we treated CD8+ T cells with ATRi (Foote *et al.*, 2018) from 0-24 h (during activation) or

125   24-48 h (during proliferation) and monitored survival using the viability dye eFluor 780. While

126   ATRi had little impact on CD8+ T cells from 0-24 h, ATRi from 24-48 h induced death in most

127   proliferating CD8$^+$ T cells (Figure 1C). We then examined whether ATRi affects the survival of

128   unactivated, naïve CD8$^+$ T cells maintained in interleukin 7 (IL-7). While ATRi caused a slight

129   decrease in the survival of naïve CD8$^+$ T cells from 0-24 h, ATRi from 24-48 h had no impact (Figure

130   1D). IL-7 can promote homeostatic proliferation and this may explain why ATRi caused a slight

131   decrease in the survival of CD8$^+$ T cells from 0-24 h (Tan et al., 2001). We also determined

132   whether a 24h treatment with ATRi impacts the survival of exponentially dividing B16 cancer cells

133   and primary fibroblasts (Figure 1E). ATRi did not induce significant cell death in B16 or primary

134   fibroblasts in 24 h. Finally, we determined whether clinical inhibitors of ATM (AZD0156), PARP

135   (Olaparib), and WEE1 (AZD1775) induced death in proliferating CD8$^+$ T cells. Neither AZD0156 nor

136   AZD1775 induced death in proliferating CD8$^+$ T cells in 24 h (Figure 1F). While Olaparib induced

137   statistically significant death in proliferating CD8$^+$ T cells, this was not comparable with ATRi

138   which induced death in most proliferating CD8$^+$ T cells in 24 h.

139   **ATR kinase is essential in previously activated, proliferating CD8$^+$ T cells *in vivo*.**

140   ATRi potentiates CD8$^+$ T cell-dependent anti-tumor activity following conformal radiation in

141   syngeneic CT26 colorectal tumors, despite transiently reducing activated CD8$^+$ T cells in BALB/c

142   host spleens (Vendetti *et al.*, 2018). To define the impact of ATRi on CD8$^+$ T cell activation and

143   proliferation *in vivo*, we treated CT26 tumor-bearing mice with 75 mg/kg of ATRi on days 1,2, and

144   3, and immunoprofiled CD8$^+$ T cells in tumor infiltrating lymphocytes (TIL) and the periphery

145   (spleen and draining lymph node (DLN)) on day 4. CD8$^+$ T cell numbers decreased in TIL in mice

146   treated with ATRi (Figure 2A). Relative CD8$^+$ T cell numbers were not changed in the periphery by

147   ATRi. However, spleen weight decreased in mice treated with ATRi (Figure S1A). Importantly, the

148   percentage of proliferating CD8$^+$ T cells (Ki67$^+$) significantly decreased in TIL, spleen, and DLN in

149   mice treated with ATRi (Figure 2B,C). Thus, ATRi impacts proliferating CD8$^+$ T cells *in vivo* in all

150   immunoprofiled tissues.

151   To determine whether ATRi impedes CD8$^+$ T cell activation *in vivo*, we examined expression of

152   the early activation marker CD69 on CD8$^+$ T cells in the TIL and periphery. The percentage of

153   newly or recently activated CD8$^+$ T cells (CD69$^+$) was increased in TIL in mice treated with ATRi

154   (Figure 2D). The percentage of recently activated CD8$^+$ T cells (CD69$^+$) in the periphery was not

155   changed by ATRi. We further probed CD8$^+$ T cell activation phenotypes using the markers CD62L

156   and CD44 to identify un-activated naïve (TN, CD26L^{lo} CD44^{lo}) CD8$^+$ T cells and activated central

157   memory (TCM, CD26L^{hi} CD44^{hi}) and effector/effector memory (TEM, CD26L^{lo} CD44^{hi}) CD8$^+$ T cells

158   in the TIL and periphery. Consistent with our previous findings (Vendetti et al., 2018), ATRi

159   reduced the percentage of activated TCM and TEM CD8$^+$ T cells in the spleen (Figure S1B,C).

160   Concurrently, ATRi increased the percentage of un-activated TN CD8$^+$ T cells in the spleen. No

161   significant changes in these populations were observed in the DLN (Figure S1B,C). While the CD8$^+$

162   TCM and TEM subpopulations in the TIL were not altered by ATRi (Figure S1B,D), the percentage

163   of total CD62L^{lo} CD8$^+$ T cells (which includes the effector/effector memory pool) decreased in TIL

164   in mice treated with ATRi (Figure S1E,F).

165   To further define the population of effector CD8$^+$ T cells impacted by ATRi *in vivo*, we examined

166   KLRG1, CD127, and CD69 expression on CD62^{lo} CD8$^+$ T cells. The percentage of short

167   lived/terminal effector CD8$^+$ T cells (KLRG1$^+$ CD127$^-$) decreased in TIL in mice treated with ATRi

168   (Figure 2E,F). Similarly, the percentage of KLRG1$^+$ effector CD8$^+$ T cells that had been previously

169   activated and had already downregulated CD69 (KLRG1$^+$ CD69$^-$) decreased in TIL in mice treated

170   with ATRi (Figure 2G,H). No significant changes in tissue resident (CD103$^+$ CD69$^+$) or memory

171   precursor effector (KLRG1$^-$ CD127$^+$) or newly activated KLRG1$^+$ effector (KLRG1$^+$ CD69$^+$) CD8$^+$ T

172   cells were seen in TIL in mice treated with ATRi (Figure S1G-J).

173   Together these data show that ATRi decreases a short-lived population of effector CD8$^+$ T cells in

174   TIL but does not impede CD8$^+$ T cell activation *in vivo*. This is entirely consistent with the data

175   presented in Figure 1 that show that CD8$^+$ T cell activation is associated with significant increases

176   in ATR and CHK1 protein expression and that ATR kinase activity is essential in activated,

177   proliferating CD8$^+$ T cells that divide 4-5 times in 24 h *ex vivo*. Thus, the impact of ATRi on CD8$^+$ T

178   cell activation and proliferation *ex vivo* is a physiologically relevant system in which to study

179   mechanism.

Most proliferating CD8$^+$ T cells are in S phase

181   We reasoned that the sensitivity of proliferating CD8$^+$ T cells to ATRi-induced cell death relative

182   to naïve CD8$^+$ T cells and other cell types (Figure 1C-E) may be associated with their rapid cell

183   cycle. To determine the cell cycle distribution of proliferating CD8$^+$ T cells, and exponentially

184   dividing primary fibroblasts and B16, we labelled S phase cells with 5-ethynyl-2'-deoxyuridine

185   (EdU) for 30 min and then identified EdU incorporation and DNA content using flow cytometry.

186   Using these datasets, we estimated the length of G1, S, and G2/M (Figure S2A). In CD8^{+} T cells,

187   G1 was ~1.0±0.3 h, S phase was ~4.7±0.3 h, and G2/M was ~0.3±0.1 h (Figure 3A). In fibroblasts,

188   G1 was ~13±3.3 h, S phase was ~8.2 h±1.8 h, and G2/M was ~7.5±2.3 h (26%) (Figure S2B). In B16,

189   G1 was ~7.1±1.3 h (41%), S phase was ~9.3±1.3 h, and G2/M was 0.7±0.3 h (Figure S2C). The cell

190   cycle distribution of these three different cell types is summarized in a figure wherein the

191   circumference of the circle represents the doubling time (Figure 3B). It is striking that most

192   proliferating CD8^{+} T cells are in S phase.

ATR kinase limits origin firing in CD8^{+} T cells

194   Next, we reasoned that ATRi-induced origin firing could cause DNA damage and death in rapidly

195   proliferating CD8^{+} T cells. In mammalian cells, CDK2 and CDC7 kinase-dependent mechanisms

196   activate the replicative helicase and initiate DNA replication at ~10% of licensed origins in a

197   spatiotemporal pattern that is broadly conserved from one cell division to the next (Cayrou et al.,

198   2011; Chagin et al., 2016). The 90% of licensed origins that are passively replicated, described as

199   either dormant or flexible origins, are essential for genome stability (Ge et al., 2007). Origin firing

200   between stalled forks is a simple way to recover replication that would otherwise be lost. In the

201   vast majority of mammalian cells, the selective pressure for genome stability likely supersedes

202   the need for rapid DNA replication and cell division. However, in effector CD8^{+} T cells the selective

203   pressure for rapid DNA replication and cell division may supersede the need for genome stability,

204   as at least 90-95% are destined to undergo cell death during contraction. We used ATRi to

205   investigate whether the fundamental mechanisms that mediate origin firing in mammalian cells

206   are conserved in proliferating CD8^{+} T cells.

207   To determine whether ATRi induces origin firing in proliferating CD8^{+} T cells, we first examined

208   the hyper-phosphorylation of chromatin bound MCM4 which has been associated with excessive

209   activation of the replicative helicase (Sheu et al., 2016). ATRi, but not ATMi or PARPi, induced a

210   mobility shift in MCM4 in chromatin extracts prepared from proliferating CD8^{+} T cells (Figure 3C).

211   WEE1i induced a mobility shift in MCM4 in chromatin extracts from proliferating CD8^{+} T cells, but

212   this was at the limits of detection. ATRi and WEE1i induce similar mobility shifts in MCM4 in

213   chromatin extracts prepared from U2OS and BJ-TERT (Moiseeva et al., 2019a). Since WEE1 is

214   highly expressed in proliferating CD8$^+$ T cells (Figure 1B), the difference is not due to an absence

215   of this kinase.

216   To determine whether ATRi induces changes in the replication timing program, we used Repli-

217   seq. Proliferating CD8$^+$ T cells were treated with ATRi for 30 min and then added 5-bromo-2-

218   deoxyuridine (BrdU) for an additional 30 min. CD8$^+$ T cells were sorted into 2N-3N and 3N-4N

219   populations and BrdU-labelled nascent DNA was purified and sequenced. ATRi did not induce late

220   origin firing in early S phase proliferating CD8$^+$ T cells (Figure 3D; Figure S3A,B). Furthermore, the

221   distribution of DNA synthesis between early and late-S phase was not significantly different

222   between fibroblasts and proliferating CD8$^+$ T cells (Figure S3C).

223   To determine whether ATRi increased DNA synthesis, we treated proliferating CD8$^+$ T cells with

224   ATRi for 30 min and then added EdU for an additional 30 min, the same incubation intervals used

225   for Repli-seq. EdU was quantitated in 2N-3N and 3N-4N cells using flow cytometry. ATRi increased

226   the relative fluorophore-EdU intensity in proliferating CD8$^+$ T cells in both in early S phase and

227   late S phase (Figure 3E). Thus, ATRi induces origin firing and increases DNA synthesis in

228   proliferating CD8$^+$ T cells without impacting the replication timing pattern.

229   **ATR kinase limits CDK1-dependent origin firing across active replicons in CD8$^+$ T cells**

230   Since ATRi increased DNA synthesis in proliferating CD8$^+$ T cells by >25% without impacting the

231   replication timing pattern, we reasoned that ATR kinase activity limits origin firing across active

232   replicons in CD8$^+$ T cells. To test this, we combed DNA purified from proliferating CD8$^+$ T cells,

233   exponentially dividing B16, and primary fibroblasts. Cells were treated with ATRi for 30 min

234   followed by 5-iodo-2-deoxyuridine (IdU) for 10 min and 5-chloro-2-deoxyuridine (CldU) for 20

235   min. ATRi decreased inter-origin distance in proliferating CD8$^+$ T cells, B16, and fibroblasts (Figure

236   3F). ATRi also decreased replication track length in proliferating CD8$^+$ T cells, B16, and fibroblasts.

237   Thus, ATRi induces dormant origin firing which increases the density and reduces the velocity of

238   replication forks in proliferating CD8$^+$ T cells.

239   ATRi-induced dormant origin firing in U2OS and BJ-TERT is associated with a CDK1-dependent

240   phosphorylation of RIF1 serine 2205 (serine-2153 in mouse) that disrupts an association between

241　RIF1 and PP1 (Moiseeva *et al.*, 2019b). RIF1 is a regulatory subunit of PP1 (Sukackaite et al., 2017)

242　and PP1 opposes CDC7 kinase activity at replication origins (Hiraga et al., 2017). To determine

243　whether these mechanisms are conserved in CD8$^+$ T cells, we treated proliferating CD8$^+$ T cells

244　with titrations of CDK1i Ro-3306, CDK2i CVT-313, and CDC7i PHA-767491 for 15 min and then

245　added ATRi for an additional 1 h. ATRi induced a mobility shift in MCM4 in chromatin extracts

246　and this was blocked by 5 µM Ro-3306 and 20 µM PHA-76749, but not by CVT-313 (Figure 3G).

247　We generated a rabbit monoclonal antibody that identifies RIF1 only when it is phosphorylated

248　on serine-2205 in human and serine-2153 in mouse (Figure S4). RIF1 phosphoserine-2153 was

249　detected in proliferating CD8$^+$ T cells and this was increased by ATRi and blocked by 5 µM Ro-

250　3306 (Figure 3H). This is the first antibody that identifies mouse RIF1. The two isoforms identified

251　here are consistent in size with those identified in mouse embryonic stem cells genetically

252　engineered to express RIF1-FLAG-HA (Sukackaite *et al.*, 2017).

253　ATR kinase-dependent CHK1 activity phosphorylates CDC25A causing its degradation in the

254　proteasome after DNA damage (Liu *et al.*, 2000; Mailand *et al.*, 2000; Sanchez *et al.*, 1997).

255　CDC25A degradation induces cell cycle arrest because inhibitory phosphorylations on CDK2 and

256　CDK1 cannot be removed (Hoffmann *et al.*, 1994). ATRi induces CDK1-dependent dormant origin

257　firing and this suggests that physiological (low level) ATR-CHK1-CDC25A signaling limits origin

258　firing by preventing CDK1 activation (Figure 3F/G). If this premise is correct, DNA damage-

259　induced (high level) ATR-CHK1-CDC25A signaling should degrade CDC25A and this should reverse

260　ATRi induced origin firing. Accordingly, the sequence of treatment with a DNA damaging agent

261　and ATRi should determine whether ATRi induces hyper-phosphorylation of chromatin bound

262　MCM4. We treated proliferating CD8$^+$ T cells and B16 with either ATRi or the ribonucleotide

263　reductase (RNR) inhibitor hydroxyurea (HU) for 30 min and then added HU or ATRi, respectively,

264　for an additional 30 min. When proliferating CD8$^+$ T cells and B16 were treated with HU before

265　ATRi, ATRi did not induce a mobility shift in MCM4 in chromatin extracts (Figure 3I). In contrast,

266　ATRi induced a mobility shift in MCM4 in chromatin extracts in proliferating CD8$^+$ T cells and B16.

267　While this mobility shift was not reversed by subsequent treatment with HU, it was reduced,

268　suggesting that free deoxyribonucleotides may be limiting for origin firing in cells treated with

269   ATRi and HU. Taken together, these data show that ATRi induces CDK1- and CDC7-kinase

270   dependent origin firing across active replicons in proliferating CD8$^+$ T cells (Figure 3J).

271   **Exogenous nucleosides rescue ATRi-induced CD8$^+$ T cell death**

272   Exogenous nucleosides rescue genome instability associated with DNA replication in pluripotent

273   stem cells and oncogene-induced senescence in primary fibroblasts cultured *in vitro* (Aird et al.,

274   2013; Halliwell et al., 2020). We hypothesized that exogenous nucleosides may rescue ATRi-

275   induced death in proliferating CD8$^+$ T cells. To test this hypothesis, we used three nucleoside

276   cocktails reported to rescue genome instability: Low rN was 250 nM adenosine (A), cytidine (C),

277   and guanosine (G), and thymidine (T)(Aird *et al.*, 2013); High rN was 15 µM A, C, and G, and 6 µM

278   T; EmbryoMax, which is marketed for mouse embryonic stem cell culture applications, was 15

279   µM A, C, G, and uridine (U), and 6 µM T (Halliwell *et al.*, 2020). We observed a dose-dependent

280   rescue of ATRi-induced death in proliferating CD8$^+$ T cells when exogenous nucleosides were

281   added to the tissue culture media 2 h prior to ATRi (Figure 4A). EmbryoMax did not rescue ATRi-

282   induced CD8$^+$ T cell death as efficiently as high rN suggesting that 15 µM U had a negative impact

283   on the survival of proliferating CD8$^+$ T cells treated with ATRi.

284   Thymidine concentrations of 1 mM or greater are used to inhibit DNA replication and arrest cells

285   at the onset of S phase and this could protect proliferating CD8$^+$ T cells from ATRi-induced death

286   (Bjursell and Reichard, 1973). We did not observe cell cycle arrest in proliferating CD8$^+$ T cells

287   treated with the nucleoside cocktails used here where the maximum concentration of thymidine

288   is 12 µM (Figure 4B; Figure S5).

289   ATRi is a competitive ATP inhibitor and the addition of exogenous nucleosides to the media could

290   block the activity of the inhibitor by, for example, preventing its transport into proliferating CD8$^+$

291   T cells (Foote *et al.*, 2018). The addition of nucleosides to proliferating CD8$^+$ T cells two hours

292   prior to ATRi did not block either the ATRi-induced mobility shift in MCM4 in the chromatin

293   fraction or the inhibition of CHK1 phosphorylation indicating that ATRi AZD6738 still enters cells

294   and is active in the presence of these concentrations of nucleosides (Figure 4C).

295   Inter-origin distance and replication fork velocity in CD8$^+$ T cells treated with ATRi were not

296   changed by the addition of nucleosides (Figure 4D). Thus, exogenous nucleosides rescue ATRi-

297   induced death in proliferating CD8$^+$ T cells in a dose-dependent manner without impacting either

298   the proliferation of cells, the activity of ATRi, or origin firing.

ATR kinase prevents thymineless death in proliferating CD8$^+$ T cells

300   To determine whether a single nucleoside could rescue ATRi-induced death in proliferating CD8$^+$

301   T cells, we treated with either 15 µM A, C, or G, or 6 µM T. Addition of 6 µM T rescued ATRi-

302   induced death in proliferating CD8$^+$ T cells with similar efficiency to high rN while addition of

303   other individual nucleosides did not significantly affect survival (Figure 5A). We did not observe

304   cell cycle arrest in proliferating CD8$^+$ T cells treated with 6 µM T (Figure 5B; Figure S6A).

305   Hydroxyurea induces ATR kinase-dependent cell cycle arrest. To determine whether ATRi and HU

306   induce death in proliferating CD8$^+$ T cells through a similar mechanism, we first determined the

307   length of treatment with ATRi and HU needed to induce death in proliferating CD8$^+$ T cells. We

308   treated proliferating CD8$^+$ T cells with thymidine and 2 h later added ATRi or 5 mM HU for 6 or 9

309   h. Cells were then replated with or without thymidine and allowed to recover to 48 h post-

310   activation.

311   ATRi for 6 h did not impact the proliferation of CD8$^+$ T cells while HU induced cell cycle arrest

312   (Figure 5C). ATRi for 6 h induced death in proliferating CD8$^+$ T cells, but while thymidine increased

313   the percentage of live cells, the change was not statistically significant (Figure S7). ATRi for 9 h

314   induced death in proliferating CD8$^+$ T cells and this was rescued by 6 µM T (Figure 5D; Figure S8).

315   In contrast, HU for 9 h induced death in proliferating CD8$^+$ T cells, and while HU-induced cell cycle

316   arrest was rescued by 6 µM T, HU-induced CD8$^+$ T cell death was not rescued by 6 µM T. We

317   conclude that the thymidine rescue of ATRi-induced death in proliferating CD8$^+$ T cells is

318   associated with proliferation and not stalled replication forks.

319   Since ATRi-induced death in proliferating CD8$^+$ T cells is associated with proliferation, we

320   hypothesized that thymidine was limiting for DNA polymerases. We therefore quantitated free

321   deoxyribonucleotide concentrations in proliferating CD8$^+$ T cells treated with ATRi or HU for 1 h.

322   Concentrations of dCTP, dCDP, dCMP, dTTP, dTDP, dTMP, and dUMP, and the concentration of

323   dUTP decreased in proliferating CD8$^+$ T cells treated with HU (Figure 6A). HU induces ATR kinase-

324   dependent cell cycle checkpoints and increases ATR kinase-dependent DCK activity for dNTP

325   salvage. Since dNTPs are not used in DNA synthesis and dNTP salvage pathways are induced in

326   proliferating CD8$^+$ T cells treated with HU, concentrations of free dCTP, dTTP, dCDP, dTDP, dCMP,

327   dTMP, and dUMP increase (Figure 6A). The concentration of dUTP decreased in proliferating CD8$^+$

328   T cells treated with HU. This suggests that DUT activity and thymidine salvage pathways were

329   induced in response to a decreased dTTP:dUTP ratio. The concentration of dUTP also decreased

330   in proliferating CD8$^+$ T cells treated with ATRi.

331   **ATR kinase prevents RRM2 and DCK degradation in the proteasome**

332   Deoxyuridine 5'-triphosphate nucleotidohydrolase (DUT) hydrolyses dUTP to dUMP and

333   pyrophosphate, simultaneously reducing dUTP and providing dUMP for dTTP biosynthesis (Figure

334   6B). A high cellular dTTP:dUTP ratio is essential to avoid dU contamination in genomic DNA. The

335   decreased concentration of free dUTP in proliferating CD8$^+$ T cells treated with ATRi suggested

336   that DUT activity had increased in response to a decreased dTTP:dUTP ratio. A key step in *de novo*

337   dTMP biosynthesis is the reduction of UDP to dUDP by RNR. ATRi's were recently reported to

338   induce CDK1-dependent phosphorylation and degradation of RRM2, a subunit of RNR, in Ewing

339   sarcoma cells, acute lymphoblastic leukemia (ALL) cells, and adrenocortical carcinoma cells

340   (Bothou et al., 2021; Koppenhafer et al., 2020; Le et al., 2017), consistent with the well-known

341   CDK1-dependent degradation of RRM2 in G2 (D'Angiolella et al., 2012). Since ATRi and HU both

342   decreased the concentration of dUTP, we hypothesized that ATRi may induce the CDK1-

343   dependent degradation of RRM2 in proliferating CD8$^+$ T cells.

344   Furthermore, the increased concentration of dCDP (dUDP is at the limits of detection) in

345   proliferating CD8$^+$ T cells treated for 1 h with HU, but not ATRi, suggested that ATR is required to

346   mitigate the consequences of RNR inhibition. A key step in dNTP salvage is the phosphorylation

347   of dA, dC, and dG by deoxycytidine kinase (DCK) to generate dAMP, dCMP, and dGMP. ATR

348   phosphorylates DCK on serine-74 and this phosphorylation is associated with DCK kinase activity

349   (Amsailale et al., 2012; Beyaert et al., 2016; Hazra et al., 2011). Since HU, but not ATRi increased

350   the concentration of dCDP, we hypothesized that ATRi inhibited DCK in proliferating CD8$^+$ T cells.

351   To test these hypotheses, we immunoblotted RRM1, RRM2, DCK, and DUT, in proliferating CD8$^+$

352   T cells treated with ATRi for 1 or 4 h. HU increased RRM2 protein levels in proliferating CD8$^+$ T

353 cells at 4 h and this was ATR kinase-dependent (Figure 6C). ATRi decreased RRM2 and DCK protein

354 levels in proliferating CD8$^+$ T cells at 1 h and 4 h. To determine whether the RRM2 and DCK were

355 degraded in the proteasome following CDK-dependent phosphorylation, we treated proliferating

356 CD8$^+$ T cells with the 5 µM MG132, a proteasome inhibitor, and 5 µM Ro-3306, for 15 min prior

357 to ATRi for 2 h. ATRi-induced a CDK1-dependent reduction in RRM2 protein and this was largely

358 via MG132-dependent degradation in the proteasome (Figure 6D). ATRi-induced a CDK1-

359 dependent reduction in DCK protein and this was entirely via MG132-dependent degradation in

360 the proteasome. The ATRi-induced reduction in RRM2 and DCK were blocked by 5 µM and 10 µM

361 CDK1i Ro-3306 (Figure 6E). The ATRi-induced reduction in RRM2 and DCK was not blocked by 5

362 µM CDK2i CVT-313 (Figure 6F).

363 To determine whether ATRi induced CDK1-dependent phosphorylation(s) on RRM2, we treated

364 proliferating CD8$^+$ T cells with ATRi, with and without CDK1i, and immunoprecipitated proteins

365 using a phospho-MAPK/CDK substrate (PXpSP or pSPXR/K) rabbit monoclonal antibody, and then

366 immunoblotted RRM2 using a rabbit polyclonal antibody and a conformation-specific HRP-

367 conjugated anti-rabbit antibody. Phosphospecific antibodies that identify RRM2

368 phosphothreonine-33 (pTPPT mouse) and phosphoserine-20 (pSPLK mouse and human), known

369 CDK-dependent sites, are not available. RRM2 was immunoprecipitated from proliferating CD8$^+$

370 T cells treated with ATRi (Figure 6G). Since the only sequence in RRM2 that matches the

371 consensus of these antibodies is phosphoserine-20, we conclude that ATRi-induced the CDK1-

372 dependent phosphorylation of pSPLK on RRM2.

373 To determine whether ATRi blocked the phosphorylation of DCK, we treated proliferating CD8$^+$ T

374 cells with ATRi, with and without CDK1i for 1 h, and immunoprecipitated proteins using a

375 phospho-SQ/phospho-TQ substrate rabbit monoclonal antibody, and immunoblotted DCK using

376 a rabbit polyclonal antibody and a conformation-specific HRP-conjugated anti-rabbit antibody.

377 Phosphospecific antibodies that identify DCK phosphoserine-74 (pSQ) are no longer available.

378 DCK was immunoprecipitated from proliferating CD8$^+$ T cells and this was blocked by ATRi (Figure

379 6H). Since the only sequence in DCK that matches the consensus of these antibodies is

380 phosphoserine-74, we conclude that DCK is phosphorylated on this site by ATR in proliferating

381 CD8$^+$ T cells.

ATR kinase is essential for genome stability in proliferating CD8$^+$ T cells

Since ATRi reduced RRM2 protein and DCK phosphorylation, and presumably their activity, in proliferating CD8$^+$ T cells, we hypothesized that ATRi may induce dU contamination in genomic DNA and genome instability. To quantitate DNA constituent base composition, we developed a fit-for-purpose LC-MS/MS assay that quantitated 1 rN per 20,000 bases from 1 mg DNA. We observed a significant increase in dU contamination, measured as the ratios of dU/dA and dU/T, in genomic DNA in proliferating CD8$^+$ T cells treated with ATRi for 1 h (Figure 7A). dU contamination in genomic DNA is repaired by base excision repair and mismatch repair, and this can generate DNA double-strand breaks at multiple damaged sites.

To determine whether ATRi induced DNA damage signaling in proliferating CD8$^+$ T cells, we quantitated γH2AX in a flow cytometry assay. We observed a dramatic increase in the number of γH2AX positive proliferating CD8$^+$ T cells treated with ATRi for 2 and 4 h (Figure 7B). Since the number of γH2AX positive proliferating CD8$^+$ T cells after treatment with ATRi for 2 and 4 h was decreased by approximately 50% by thymidine, we reasoned that a second class of lesion might also cause cell death.

We hypothesized that ATRi-induced dormant origin firing in genes may result in both R loops at sites of transcription and primer synthesis. To test this hypothesis, we generated genomic DNA from B16 and proliferating CD8$^+$ T cells treated with the topoisomerase inhibitor camptothecin (TOP1i) or ATRi for 1 h using conditions that preserve R loops and RNA primers (Chedin et al., 2021; Ginno et al., 2012). We immunopurified RNA-DNA hybrids from restriction endonuclease digested DNA using S9.6 and after extensive washing liberated the DNA from beads using proteinase K. Denatured DNA was dot blotted using an anti-single-stranded DNA antibody. RNA-DNA hybrids were induced by both TOP1i and ATRi (Figure 7C).

Origins preferentially fire in gene promoters rather than gene coding regions (Chen et al., 2019; Petryk et al., 2016). Transcription starts in early G1 phase, peaks at the G1/S boundary, and then fades during the early stages of S phase (Bertoli et al., 2013). These mechanisms that coordinate transcription and DNA replication may be critical in proliferating CD8$^+$ T cells that have a short G1 phase (Figure 3A-B). We used the proximity ligation assay (PLA) to quantitate collisions between

410   DNA replication (identified by PCNA) and RNA transcription (identified by RNA polymerase II (Pol

411   II) phosphoserine-5) complexes. We observed an increase in PCNA-RNA polymerase PLA signals

412   in proliferating CD8$^+$ T cells treated with ATRi for 1 h (Figure 7D). This increase in PCNA-RNA

413   polymerase-PCNA PLA signals was observed in both S phase cells (EdU$^+$) and, to a lesser extent,

414   EdU$^-$ cells. However, CD8$^+$ T cells divide extremely fast, and during a 1 h treatment with ATRi,

415   ~20 % of cells are anticipated to exit S phase (~4.7±0.3 h/1 h).

DISCUSSION

417   ATRi's have advanced to phase 1 and phase 2 trials and NCI's Experimental Therapeutics Network

418   has formed Project Teams to develop and prioritize ATRi's in clinical trials. In this study, we show

419   that ATRi induces untimely CDK1 activity in S phase in proliferating CD8$^+$ T cells, and that this

420   induces origin firing across active replicons and simultaneous degradation of dNTP synthesis and

421   salvage enzymes. These effects of ATRi in proliferating CD8$^+$ T cells lead to dU contamination in

422   genomic DNA, R loops, transcription-DNA replication machinery collisions, and death in

423   proliferating CD8$^+$ T cells, but not in naïve CD8$^+$ T cells, B16 melanoma, or primary fibroblasts

424   after a 24 h treatment. ATRi-induced death in proliferating CD8$^+$ T cells was significantly rescued

425   by thymidine treatment. This may provide an explanation for how ATRi's suppress proliferating T

426   cells causing dose-limiting toxicity in patients.

427   ATRi's are not inert agents that only have activity when combined with a DNA damaging agent.

428   ATRi's fundamentally change DNA replication in cells and the effect is greater in proliferating

429   CD8$^+$ T cells than naïve CD8$^+$ T and cancer cells. Thus, ATRi's may cause transient leukocytopenia

430   without impacting naïve populations, allowing rebound proliferation of immune cell populations

431   in both the tumor microenvironment (TME) and periphery. In the TME, many sub-populations of

432   T cells in various degrees of dysfunction (exhausted T cells, regulatory T cells) are being

433   continuously stimulated to proliferate. This *in situ* proliferative signal may represent an

434   unappreciated target of ATRi's, such that certain populations are selectively targeted due to their

435   underlying proliferation and replicative stress. Furthermore, recent preclinical studies

436   demonstrate that ATRi's potentiates type I interferon (IFN1) signaling, production of pro-

437   inflammatory cytokines/chemokines, myeloid immune cell infiltration, and antigen presentation

438   after radiation (Dillon et al., 2019; Feng et al., 2020). Taken with our previous findings that ATRi

439   and radiation promote CD8^{+} T cell-dependent anti-tumor responses (Vendetti *et al.*, 2018), these

440   studies collectively link DNA damage following ATRi and radiation, pro-inflammatory cytokine

441   signaling, recruitment and activation of the innate immune system, and activation of the adaptive

442   immune system to mediate anti-tumor responses.

443   Our observation that ATR limits origin firing across active replicons in proliferating mouse CD8^{+} T

444   cells *ex vivo*, as well as in mouse and human cancer cell lines and fibroblasts, argues that the

445   underlying mechanism is fundamental to DNA replication in these species. Consistent with this

446   premise, we show that ATRi induces a CDK1 kinase-dependent phosphorylation on RIF1 serine-

447   2153 (serine-2205 human) in proliferating CD8^{+} T cells. We previously showed that RIF1 serine-

448   2205 phosphorylation disrupts an association between PP1 and RIF1 in human U2OS and BJ-TERT

449   (Moiseeva *et al.*, 2019b). Others showed that PP1 opposes CDC7 kinase-dependent origin firing

450   in human cells (Hiraga *et al.*, 2017). Taken together, these data are consistent with a model in

451   which ATR-CHK1-CDC25A signaling prevents the CDK1 kinase-dependent phosphorylation on

452   RIF1 that would disrupt the localization of PP1 that opposes CDC7-dependent origin firing across

453   active replicons. Accordingly, ATRi induces the CDK1 kinase-dependent phosphorylation on RIF1

454   and this disrupts the localization of PP1, causing CDC7-dependent origin firing across active

455   replicons (Figure 7F, right). In this model, ATR signaling limits origin firing in the absence of either

456   DNA lesions or mechanical failures.

457   Our data showing that HU and ATRi have different effects in proliferating CD8^{+} T cells are entirely

458   consistent with the model suggested above. HU inhibits RNR activating a DDR that is anticipated

459   to induce ATR-CHK1-CDC25A-dependent cell cycle checkpoints (Figure 5C) and increase ATR

460   kinase-dependent DCK activity for dNTP salvage. Since dNTPs are not used in DNA synthesis and

461   dNTP salvage pathways are induced in proliferating CD8^{+} T cells treated with HU, concentrations

462   of free dCTP, dTTP, dCDP, dTDP, dCMP, dTMP, and dUMP increase (Figure 6A). The decreased

463   concentration of dUTP in proliferating CD8^{+} T cells treated with HU (Figure 6A) suggests that DUT

464   activity was increased in response to a decreased dTTP:dUTP ratio. While mechanisms that

465   control DUT activity are not known, DUT hydrolyses dUTP to dUMP and pyrophosphate,

466   simultaneously reducing dUTP to prevent dU contamination in genomic DNA and providing

467   dUMP for the *de novo* synthesis of dTTP.

468   ATRi inhibits DCK (Figure 6H) and induces untimely CDK1 activity during S phase in proliferating

469   CD8$^+$ T cells, and this increases DNA synthesis (Figure 3E) and causes RRM2 and DCK degradation

470   in the proteasome (Figure 6C). Remarkably, these effects do not cause cell cycle arrest (Figure

471   5C), or change dCTP, dTTP, dCDP, dTDP, dCMP, dTMP, and dUMP concentrations in proliferating

472   CD8$^+$ T cells at 1 h (Figure 6A). The decreased concentration of dUTP in proliferating CD8$^+$ T cells

473   treated with ATRi (Figure 6A) suggests that DUT activity had increased in response to a decreased

474   dTTP:dUTP ratio. Our observation that the decrease in the concentration of dUTP in CD8$^+$ T cells

475   treated with ATRi was less than those treated with HU, suggesting that ATR may be required to

476   increase DUT activity in response to a decreased dTTP:dUTP ratio. The increased DNA synthesis,

477   and modest decrease in the concentration of free dUTP, could explain why dU contamination in

478   genomic DNA is observed in proliferating CD8$^+$ T cells treated with ATRi, but not HU (Figure 7A).

479   dU contamination in genomic DNA is repaired by base excision repair (BER) mechanisms initiated

480   by uracil DNA glycosylases, primarily UNG, and mismatch repair (MMR). The removal of uracil by

481   UNG generates an abasic site which is cleaved by APE1 to generate a single-strand break (SSBs).

482   ATRi's are anticipated to concentrate dU contamination in genomic DNA at replication forks, and

483   the concentration of dU contamination may be further increased by futile cycles of BER repair

484   synthesis when the dTTP:dUTP ratio is low. This could result in APE1-induced SSBs on opposite

485   strands of the helix that generate DSBs at multiple damaged sites, and subsequently, cell death.

486   This is entirely consistent with our observation of that ATRi induced γH2AX in proliferating CD8$^+$

487   T cells at 2 and 4 h (Figure 7B). Since the number of γH2AX positive proliferating CD8$^+$ T cells

488   treated with ATRi decreased by approximately 50% by thymidine, we reasoned that a second

489   class of lesion might also cause cell death.

490   In addition to our observation that ATRi induce dU contamination in genomic DNA, we also found

491   that ATRi induce R loops and transcription-DNA replication machinery collisions in proliferating

492   CD8$^+$ T cells. We anticipate that the extent to which ATRi will induce dU contamination in genomic

493   DNA in cells is a function of the amount of ongoing DNA synthesis, determined by both the length

494   of S phase and the rate of dTTP biosynthesis. We anticipate that the extent to which ATRi will

495   induce R loops and DNA polymerase-RNA polymerase machinery collisions in cells is a function

496   of the separation of RNA and DNA synthesis, determined by the relative length of S and G1 phase.

497   As G1 is abridged to approximately 1 h in proliferating CD8$^+$ T cells, most of the transcription must

498   be concomitant with DNA replication. This is a fundamental difference between proliferating

499   CD8$^+$ T cells, and cancer cells and fibroblasts. Pol II can synthesize 70 bp/sec and e.g. it would

500   take Pol II approximately 44 min to transcribe just ATM (184,490 bp) without pausing (Darzacq

501   et al., 2007). Accordingly, the number of active RNA polymerases and DNA polymerases in genes

502   is likely to be greater in proliferating CD8$^+$ T cells than cancer cells or fibroblasts, and the number

503   of ATRi-induced R loops and DNA polymerase-RNA polymerase machinery collisions is likely to

504   be higher. Further work is needed to quantitate ATRi-induced DNA damage in different cell types.

505   In summary, our work serves to highlight the direct impact of ATRi in CD8$^+$ T cells and points to a

506   role for ATRi's as immune modulators. Our work also provides novel insights for the

507   combinatorial application of ATRi with genotoxic therapies, including anti-metabolites, and

508   immunotherapies in a clinical setting. Considering the wide interest in ATRi, CHK1i and WEE1i,

509   which have a similar impact on origin firing in cancer cells, our insights may be used to design

510   novel therapeutic approaches aimed at generating anti-tumor immunity.

511   **MATERIALS AND METHODS**

512   Antibodies

513   Antibodies used in this study are summarized in Table SM1.

514   Inhibitors

515   AZD6738, AZD0156, Olaparib, and AZD1775 were provided by AstraZeneca. Other inhibitors used

516   in this study are Ro-3306 (CDK1i, Selleckchem S7747), CVT-313 (CDK2i, Santa Cruz 199986-75-9),

517   PHA-767491 (CDC7i, Selleckchem S2742), (S)-(+)-camptothecin (TOP1i, MilliporeSigma C9911),

518   and MG132 (proteasome inhibitor, Selleckchem S2619).

519   Mice

520   C57BL/6, Pmel-1 TCR transgenic (B6.Cg-*Thy1^a*/Cy Tg(TcraTcrb)8Rest/J), and female BALB/c mice

521   were purchased from Jackson Laboratories.

522   Cell lines

523   B16-F10 (ATCC CRL-6475) and CT26 (ATCC CRL-2638) were cultured in DMEM and RPMI,

524   respectively, containing 10 % FBS, 100 U/mL penicillin and 100 mg/mL streptomycin (all Lonza).

525   Cells were routinely tested for mycoplasma.

Primary fibroblasts isolation and culture

527   Primary fibroblasts were isolated from the ears of 6-8 week Pmel-1 mice as described previously

528   (Khan and Gasser, 2016). Fibroblasts were cultured in DMEM containing 15 % FBS, 100 U/mL

529   penicillin, 100 mg/mL streptomycin (all Lonza), 1x MEM NEAA, 1 mM sodium pyruvate, 25 mM

530   HEPES pH 8.0, 120 µM β-mercaptoethanol (all Gibco), and 250 ng/mL amphotericin-B (Sigma-

531   Aldrich).

CD8$^+$ T cell isolation, activation, and culture

533   CD8$^+$ T cells were extracted from spleen and lymph nodes of 6-8 week C57BL/6 and Pmel-1 mice.

534   To obtain single cell suspension, spleens and lymph nodes were mechanically processed between

535   frosted glass slides and filtered through 70 µm cell strainers (Corning). Erythrocytes were lysed

536   in 150 mM NH$_4$Cl, 10 mM NaHCO$_3$, 0.1 mM EDTA pH 8.0. Pmel-1 CD8$^+$ T cells were activated by

537   incubating with R10 media (RPMI containing 10 % FBS, 100 U/mL penicillin and 100 mg/mL

538   streptomycin (all Lonza), 1x MEM NEAA, 1 mM sodium pyruvate, 5 mM HEPES pH 8.0, 50 µM β-

539   mercaptoethanol (all Gibco)) supplemented with 1 µM human gp100 (25-33) (Eurogentec) and

540   50 U/mL IL-2 (PeproTech) for 24 h. Naïve CD8$^+$ T cells were cultured in R10 media containing 5

541   ng/mL IL-7 (R&D systems). C57BL/6 CD8$^+$ T cells were purified using the EasySep Mouse CD8 T

542   Cell Isolation Kit (Stemcell technologies) according to the manufacturer's instructions. C57BL/6

543   CD8$^+$ T cells were activated by resuspending into R10 media containing 50 U/mL IL-2 (PeproTech)

544   and 2 µg/mL anti-CD28 antibody (BD) and then plated in a culture plate pre-coated with 10 µg/mL

545   anti-CD3$_\varepsilon$ antibody (Biolegend). Culture medium was exchanged to R10 containing IL-2 and the

546   cell density was adjusted to be 0.5 – 1x10^6 cells/ml every 24 h.

Proliferation and survival assays

548   For the proliferation assay, 5x10^6 cells/mL were stained in 8 mg/mL Cell Trace Violet (CTV, Fisher)

549   in PBS for 10 min. Staining was quenched the addition of with 5x the volume of R10 media and

550   then activated as above. Cells were collected on ice and surface antigens were identified using

551   the antibodies indicated (Table SM1) for 15 min before staining for 10 min with eFluor780

552   viability dye (1:4000, ThermoFisher). Cells were fixed in Fixation/Permeabilization reagent

553   (eBioscience) and uncompensated data was collected using a LSRFortessa cytometer and

554   FACSDiva Software (BD Biosciences). Compensation and analyses were performed using FlowJo

555   v10 software. Gating is shown in Figure SM1.

556   <u>Nuclease insoluble chromatin fractionation and immunoblotting</u>

557   Purification of nuclease insoluble chromatin (NIC) and immunoblotting of hyper-

558   phosphorylationMCM4 was performed as described previously (Moiseeva *et al.*, 2017). Soluble

559   fractions were blotted for the antibodies listed in Table SM1.

560   <u>*In vivo* treatments and immunophenotyping</u>

561   CT26 cells (approximately 5×10^5 in RPMI) were subcutaneously injected into the right hind flank

562   of 8-10 week old mice. Treatment started 7-10 days later when tumors reached ~60-120 mm^3.

563   Mice were treated daily for 3 days with 75 mg/kg AZD6738 or vehicle in a volume of 10 µL/g of

564   bodyweight, as described previously (Vendetti *et al.*, 2018). AZD6738 was dosed (in 50 % H$_2$O,

565   40 % Propylene Glycol, 10 % DMSO) by oral gavage. Spleens, tumor-draining lymph nodes (DLN,

566   right inguinal) and CT26 tumors were excised from mice at day 4. Tissues were processed to

567   generate single cell suspensions, as described previously (Vendetti *et al.*, 2018). Briefly, spleens

568   and DLN were mechanically dissociated between frosted glass slides and filtered through 70 µm

569   cell strainers (Corning). Tumors were injected in multiple locations with a total of 1.5 mL RPMI

570   containing 50 µg/mL Liberase DL research grade (Roche) and 10 U/mL DNase I (Sigma), incubated

571   3 min at room temperature, cut into small pieces, incubated in a total volume of 5 mL Liberase

572   DL/DNase solution for 15 min at 37°C, mechanically dissociated between frosted glass slides,

573   filtered through 70 µm cell strainers (Corning), vortexed at low speed for 90 sec, and filtered

574   again through new 70 µm cell strainers (Corning). Erythrocytes were lysed in 150 mM NH$_4$Cl, 10

575   mM NaHCO$_3$, 0.1 mM EDTA pH 8.0. for 30 sec (spleens) or 10 sec (tumors). Cells suspensions

576   were counted using a Scepter 2.0 or 3.0 handheld counter (Millipore) and seeded at 1.5×10^6

577   cells in 96-well round bottom plates for staining. Cells were blocked in FSC buffer (2% FBS/1x PBS)

578   containing 0.5 µg anti-CD16/32 antibody (TruStain FcX Plus, BioLegend) for 10 min at 4°C to block

579   non-specific binding of antibodies via Fc receptors, stained in FSC buffer containing antibodies to

580   surface antigens, Brilliant Stain Buffer Plus (1:5, BD Biosciences), and True-Stain Monocyte

581   Blocker (1:20, BioLegend) for 15 min at 4°C, stained with eFlour780 viability dye (1:4000,

582   ThermoFisher) for 10 minutes at 4°C to label dead/dying cells, fixed and permeabilized in

583   eBioscience Fixation/Permeabilization reagent (ThermoFisher) for 15 min at room temperature,

584   and when performing nuclear staining of Ki67, stained for 45 min at room temperature in

585   eBioscience 1x Permeabilization Buffer (ThermoFisher) containing anti-mouse Ki67 antibody.

586   Uncompensated data were collected with a BD LSRFortessa 4-laser cytometer and BD FACSDiva

587   software. Compensation and data analyses were performed in FlowJo V10 software. Single color

588   compensation controls included single stained OneComp eBeads (ThermoFisher) and single

589   stained spleen or DLN samples and matching unstained cells. Fluorescence minus one (FMO)

590   controls were included where appropriate to empirically determine gating. Antibody panel for

591   surface antigens are shown in Table SM1 and gating strategies are shown in Figures SM2/3.

592   Cell cycle analysis

593   For cell cycle analysis, asynchronous populations of the cells were labeled with 10 µM EdU for 30

594   minutes at 37 °C. Cells were harvested, washed with PBS, and fixed in cold 70 % ethanol on ice

595   for 30 minutes. Fixed cells were permeabilized using 1x Saponin permeating solution (Alfa Aesar)

596   diluted in 1% BSA in PBS for 15 min. EdU was identified using EdU Click-It kit (Thermofisher,

597   C10632) according to the manufacturer's instructions. EdU-labeled cells were washed with 1x

598   Saponin permeating solution and resuspended in 200 – 300 µl PBS containing 200 nM FxCycle^{TM}

599   Far Red Stain (Thermofisher, F10348) and 0.1 mg/mL RNase A (Thermo Scientific, EN0531. Data

600   were collected with a Accuri C6 cytometer and software (BD Biosciences). Data analyses were

601   performed using Flowjo v10 software.

602   Repli-seq

603   Library preparation was performed as described previously (Moiseeva et al., 2019a). Sequencing

604   was performed on an Illumina HiSeq (GENEWIZ). Raw Repli-seq reads were trimmed and filtered

605   for quality using Trim Galore

606   (https://www.bioinformatics.babraham.ac.uk/projects/trim_galore/). Reads were aligned using

607 bowtie2 (Langmead and Salzberg, 2012) against GRCm38 (mm10). Genome-wide RT profiles

608 were constructed, scaled, and pooled for analysis, as described previously (Marchal et al., 2018).

609 Briefly, Log2 ratios of early versus late read counts were calculated for 50kb non-overlapping

610 windows, Loess smoothed at 300kb windows. Data were visualized using IGV (Robinson et al.,

611 2011). Repli-seq data have been deposited in the Gene Expression Omnibus database (accession

612 no. GSE183412).

613 <u>DNA combing</u>

614 30 minutes post treatment, 25 μM IdU was added for 10 minutes followed by 200 μM CldU for

615 20 minutes (both MP Biomedical). Cells were harvested and washed twice with PBS. Cells were

616 then resuspended in PBS, mixed with an equal volume of 1 % low melting point agarose (Bio-Rad,

617 161-3111), and allowed to solidify in plug molds (Bio-Rad, 170-3713). Agarose plugs were

618 incubated in 2 mg/mL proteinase K, 50 mM EDTA, 1 % Sarkosyl, and 10 mM Tris pH 7.5 overnight

619 at 50 °C. The buffer was replaced and the incubation was continued for an additional 6 h. Plugs

620 were washed 5 times in TE50 (10 mM Tris-HCl pH 7.0, 50 mM EDTA) and stored at 4 °C or washed

621 3 more times in TE (10 mM Tris-HCl pH 8.0, 1 mM EDTA). Each plug was melted in 200 μl TE at

622 68 °C for 30 minutes and then digested using β-agarase I (BioLabs, M0392L) at 42 °C overnight.

623 MES buffer, pH 5.5 was gently added to increase the volume to 2 mL and the mixture was

624 incubated at 68 °C 30 min. DNA was combed onto CombiCoverslips^{TM} using the molecular

625 combing system (Genomic Vision). Cover slips were baked for 2 h at 60 °C. DNA strands were

626 denatured in 1 M NaOH and 1.5 M NaCl for 8 min, neutralized in PBS, and dehydrated with

627 subsequent 5 minutes incubations with 70, 90, and 100 % ethanol. Halogenated nucleotides were

628 identified with anti-IdU (1:20, BD Biosciences, 347580) and anti-CldU (1:50, Abcam, ab6326)

629 antibodies for 1 h at 37 °C. Slides were then stained with anti-mouse Alexa 594 (1:50, Invitrogen,

630 A11005) and anti-rat Alexa 488 (1:50, Invitrogen, A21470), followed by anti-ssDNA (1:50,

631 Millipore, MAB3034), and then anti-mouse Alexa 647 (1:50, Invitrogen, A21235), each incubated

632 for 30 min. Slides were dehydrated in ethanol as described above and mounted using ProLong^{TM}

633 Diamond Antifade Mountant with DAPI (Invitrogen, P36971). DNA fiber images were acquired

634 with a Nikon Ti inverted fluorescence microscope using NIS Elements v5.3 at 60x magnification

635 and analyzed using Adobe Photoshop Elements 15 and ImageJ software.

636 Quantification of free nucleotides by LC-HRMS

637 Nucleotides were analyzed from cells by LC-HRMS as previously described (Kuskovsky et al., 2019).

638 Cell pellets were extracted by addition of a 50 μL (20 ng/μL) mix of all stable isotope labeled

639 internal standards (1000 ng/sample) in 80:20 (v/v) methanol:water followed by 1 mL of −80 °C

640 80:20 (v/v) methanol:water before homogenization by probe tip sonication, incubation at −80 °C

641 for 30 min, centrifugation at 17,000 rcf for 10 minutes at 4°C, evaporation of the supernatant to

642 dryness, then resuspended in 50 μL 95:5 water: methanol. An Ultimate 3000 UHPLC equipped

643 with an autosampler kept at 6°C and a column heater kept at 55°C using a HSS C18 column (2.1

644 × 100 mm i.d., 3.5 μm; Waters) was used for separations. Solvent A was 5 mM DIPEA and 200

645 mM HFIP and solvent B was methanol with 5 mM DIPEA 200 mM HFIP. The gradient was as

646 follows: 100% A for 3 min at 0.18 mL/min, 100% A at 6 min with 0.2 mL/min, 98% A at 8 min with

647 0.2 mL/min, 86% A at 12 min with 0.2 mL/min, 40% A at 16 min and 1% A at 17.9 min-18.5 min

648 with 0.3 mL/min then increased to 0.4 mL/min until 20 min. Flow was ramped down to 0.18

649 mL/min back to 100% A over a 5 min re-equilibration. For MS analysis, the UHPLC was coupled

650 to a Q Exactive HF mass spectrometer (Thermo Scientific) equipped with a HESI II source

651 operating in negative mode. The operating conditions were as follows: spray voltage 4000 V;

652 vaporizer temperature 200°C; capillary temperature 350°C; S-lens 60; in-source CID 1.0 eV,

653 resolution 60,000. The sheath gas (nitrogen) and auxiliary gas (nitrogen) pressures were 45 and

654 10 (arbitrary units), respectively. Single ion monitoring (SIM) windows were acquired around the

655 [M-H]- of each analyte with a 20 m/z isolation window, 4 m/z isolation window offset, 1e6 ACG

656 target and 80 ms IT, alternating in a Full MS scan from 70-950 m/z with 1e6 ACG, and 100 ms IT.

657 Data was analyzed in XCalibur v4.0 and/or Tracefinder v5.1 (Thermo Scientific) using a 5 ppm

658 window for integration of the peak area of all analytes. Standards used as calibrants and isotope

659 labeled internal standards are indicated in the Table SM2, all were used without further

660 purification, and no adequate commercially available diphosphate standard was found therefore

661 the monophosphate was used as a surrogate standard.

662 Quantification of nucleosides incorporated into the genome

663 Cells were resuspended in TE buffer containing 62.5 μg/mL proteinase K (Invitrogen, AM2546),

664 62.5 μg/mL RNase A (Thermo Scientific, EN0531), and 0.5 % SDS and incubated overnight at 37 °C.

665 Genomic DNA was purified by phenol/chloroform extraction and resuspended in RNase/DNase

666 free water. 5 µg DNA was digested with 5 µl RNase H (NEB, M0297), 3 µl Hind III (Fisher, FD0504),

667 3 µl EcoRI (Fisher, FD0274), and 3 µl Bam HI (Fisher, FD0054) in RNase H buffer (NEB, M0297)

668 overnight at 37 °C. Digested DNA was purified using the GeneJET PCR Purification Kit (Thermo

669 Scientific, K0702). DNA was further digested into single nucleosides using DNA Degradase Plus

670 (Zymo Research, E2021).

671 To quantitate DNA constituent base composition, a fit-for-purpose LC-MS/MS assay was

672 implemented on a 1290 Infinity II Autosampler and Binary Pump and a SCIEX 6500+ triple

673 quadrupole mass spectrometer. Chromatographic separation was conducted on an Inertsil ODS-

674 3 (3 µm x 100 mm 2.1 mm) reverse phase column at ambient temperature with a gradient mobile

675 phase of methanol and water with 0.1% formic acid. MRM transitions of all analytes and isotopic

676 internal standards were monitored to construct calibration curves. We were able to quantitate

677 1 rN per 20,000 bases from 1 mg DNA.

678 <u>R-loop purification and dot blot</u>

679 Genomic DNA was prepared as above. 5 µg DNA was digested with 3 µl Hind III (Fisher, FD0504),

680 3 µl EcoRI (Fisher, FD0274), and 3 µl Bam HI (Fisher, FD0054) +/-5 µl RNase H (NEB, M0297) in

681 RNase H buffer (NEB, M0297) overnight at 37 °C. Digested DNA was incubated with 50 µl of

682 protein A/G agarose beads (Santa Cruz, sc-2003) and 10 ul mouse serum (MP Biomedicals,

683 152282) in 1.5 mL PBS/0.5% Triton X100 for 2 h at 4 °C. Digested DNA was then incubated with

684 50 µl of protein A/G agarose beads and 5 µl anti-S9.6 (Millipore, MABE1095) overnight at 4 °C.

685 Agarose beads were washed 3x for 3 min in PBS/0.5% Triton X100 binding buffer followed by PBS

686 wash for 3 min. The beads were then incubated with 3 µl proteinase K for 2 h at 37 °C. Nucleic

687 acids were purified by phenol/chloroform extraction and ethanol precipitation. DNA was

688 denatured in 50 µl TE and mixed with 50 µl of 0.8 M NaOH/20 mM EDTA solution for 10 min at

689 95°C then placed on ice. The solution was neutralized using sodium acetate pH 7.0 and DNA

690 sample was transferred to Whatman Hybond N+ Blotting Membrane (Millipore Sigma, Z761079).

691 Nucleic acids were cross-linked by to the membrane by baking at 60 °C for 30 min followed by

692 UV exposure. The membrane was blocked for 1 h with 5 % milk in TBST and blotted for anti-

693 ssDNA (1:1000, Millipore, MAB3034).

694 ɣH2AX analyses

695 Cells were harvested, washed with PBS, and fixed in cold 70 % ethanol on ice for 30 minutes for

696 immediate staining or stored at -20 °C until use. Fixed cells were washed with PBS and

697 permeabilized using 1x Saponin permeating solution (Alfa Aesar) diluted in 1% BSA in PBS for 15

698 min. Cells were stained with FITC anti-mouse ɣH2AX (1:250 in FCS buffer) for 30 min. ɣH2AX-

699 labeled cells were washed with 1x Saponin permeating solution and resuspended in 200 – 300 µl

700 PBS containing 200 nM FxCycle^{TM} Far Red Stain (Thermofisher, F10348) and 0.1 mg/mL RNase A

701 (Thermo Scientific, EN0531). Data were collected with a Accuri C6 cytometer and software (BD

702 Biosciences). Data analyses were performed using Flowjo v10 software.

703 Proximity ligation assay (PLA)

704 After treatment, cells were collected on glass slides using a cytospin (Thermo Scientific) at 2000

705 rpm for 10 min. Cells were fixed with 4 % paraformaldehyde in PBS for 15 min and permeabilized

706 in 0.1 % Triton X-100 for 10 min. Cells were washed with PBS, blocked with the blocking solution

707 (Duolink) for 1 h and incubated overnight with anti-PCNA (1:5,000, ab 92552 (AbCam)) and anti-

708 phospho-RNA polymerase II (S5) (1:100,000, ab5408 (AbCam)) in the Ab diluent solution

709 (Duolink) at 4 °C. PLA reactions were performed using the following kits from Duolink: anti-rabbit

710 PLUS (DUO92002), anti-mouse MUNUS (DUO92004), PLA detection reagent RED (DUO92008),

711 and wash buffers, fluorescence (DUO8249). Slides were washed with PBS and EdU-labeled using

712 EdU Click-It kit (Thermofisher, C10632). Cells were mounted using ProLong^{TM} Diamond Antifade

713 Mountant with DAPI (Invitrogen, P36971). Images were acquired with a Nikon Ti inverted

714 fluorescence microscope using NIS Elements v5.3 at 60x magnification and analyzed using Adobe

715 Photoshop Elements 15 and ImageJ software.

716 Study approval

717 Experimental procedures were approved by the University of Pittsburgh Animal Care and Use

718 Committees and performed in accordance with the relevant guidelines and regulations.

719 **ACKNOWLEDGEMENTS**

726   **AUTHOR CONTRIBUTIONS**

727   NS, FPV, AJC, JJD, SSH, DP, AB, YNG, and CJB designed, performed, and analyzed experiments.

728   HUO, NWS, and JHB designed and analyzed experiments. TNM, YW, YNG, KMA, and GMD made

729   significant academic contributions. NS, FPV, AJC, and CJB wrote the paper.

730   **CONFLICT OF INTEREST**

731   The authors declare no competing interests.

732   **REFERENCES**

733   Aird, K.M., Zhang, G., Li, H., Tu, Z., Bitler, B.G., Garipov, A., Wu, H., Wei, Z., Wagner, S.N., Herlyn,
734   M., and Zhang, R. (2013). Suppression of nucleotide metabolism underlies the establishment
735   and maintenance of oncogene-induced senescence. Cell reports *3*, 1252-1265.
736   10.1016/j.celrep.2013.03.004.
737   Amsailale, R., Van Den Neste, E., Arts, A., Starczewska, E., Bontemps, F., and Smal, C. (2012).
738   Phosphorylation of deoxycytidine kinase on Ser-74: impact on kinetic properties and nucleoside
739   analog activation in cancer cells. Biochem Pharmacol *84*, 43-51. 10.1016/j.bcp.2012.03.022.
740   Bertoli, C., Skotheim, J.M., and de Bruin, R.A. (2013). Control of cell cycle transcription during
741   G1 and S phases. Nat Rev Mol Cell Biol *14*, 518-528. 10.1038/nrm3629.
742   Beyaert, M., Starczewska, E., Van Den Neste, E., and Bontemps, F. (2016). A crucial role for ATR
743   in the regulation of deoxycytidine kinase activity. Biochem Pharmacol *100*, 40-50.
744   10.1016/j.bcp.2015.11.022.
745   Bjursell, G., and Reichard, P. (1973). Effects of thymidine on deoxyribonucleoside triphosphate
746   pools and deoxyribonucleic acid synthesis in Chinese hamster ovary cells. J Biol Chem *248*,
747   3904-3909.
748   Bothou, C., Sharma, A., Oo, A., Kim, B., Perge, P., Igaz, P., Ronchi, C.L., Shapiro, I., and Hantel, C.
749   (2021). Novel Insights into the Molecular Regulation of Ribonucleotide Reductase in
750   Adrenocortical Carcinoma Treatment. Cancers (Basel) *13*. 10.3390/cancers13164200.
751   Bracci, L., Schiavoni, G., Sistigu, A., and Belardelli, F. (2014). Immune-based mechanisms of
752   cytotoxic chemotherapy: implications for the design of novel and rationale-based combined
753   treatments against cancer. Cell Death Differ *21*, 15-25. 10.1038/cdd.2013.67.
754   Brown, E.J., and Baltimore, D. (2000). ATR disruption leads to chromosomal fragmentation and
755   early embryonic lethality. Genes & development *14*, 397-402.

756 Cayrou, C., Coulombe, P., Vigneron, A., Stanojcic, S., Ganier, O., Peiffer, I., Rivals, E., Puy, A.,
757 Laurent-Chabalier, S., Desprat, R., and Mechali, M. (2011). Genome-scale analysis of metazoan
758 replication origins reveals their organization in specific but flexible sites defined by conserved
759 features. Genome research *21*, 1438-1449. 10.1101/gr.121830.111.
760 Chagin, V.O., Casas-Delucchi, C.S., Reinhart, M., Schermelleh, L., Markaki, Y., Maiser, A., Bolius,
761 J.J., Bensimon, A., Fillies, M., Domaing, P., et al. (2016). 4D Visualization of replication foci in
762 mammalian cells corresponding to individual replicons. Nat Commun *7*, 11231.
763 10.1038/ncomms11231.
764 Chedin, F., Hartono, S.R., Sanz, L.A., and Vanoosthuyse, V. (2021). Best practices for the
765 visualization, mapping, and manipulation of R-loops. EMBO J *40*, e106394.
766 10.15252/embj.2020106394.
767 Chen, Y.H., Keegan, S., Kahli, M., Tonzi, P., Fenyo, D., Huang, T.T., and Smith, D.J. (2019).
768 Transcription shapes DNA replication initiation and termination in human cells. Nat Struct Mol
769 Biol *26*, 67-77. 10.1038/s41594-018-0171-0.
770 Ciccia, A., and Elledge, S.J. (2010). The DNA damage response: making it safe to play with
771 knives. Mol Cell *40*, 179-204. 10.1016/j.molcel.2010.09.019.
772 Cortez, D., Guntuku, S., Qin, J., and Elledge, S.J. (2001). ATR and ATRIP: partners in checkpoint
773 signaling. Science *294*, 1713-1716. 10.1126/science.1065521.
774 Couch, F.B., Bansbach, C.E., Driscoll, R., Luzwick, J.W., Glick, G.G., Betous, R., Carroll, C.M., Jung,
775 S.Y., Qin, J., Cimprich, K.A., and Cortez, D. (2013). ATR phosphorylates SMARCAL1 to prevent
776 replication fork collapse. Genes & development *27*, 1610-1623. 10.1101/gad.214080.113.
777 D'Angiolella, V., Donato, V., Forrester, F.M., Jeong, Y.T., Pellacani, C., Kudo, Y., Saraf, A., Florens,
778 L., Washburn, M.P., and Pagano, M. (2012). Cyclin F-mediated degradation of ribonucleotide
779 reductase M2 controls genome integrity and DNA repair. Cell *149*, 1023-1034.
780 10.1016/j.cell.2012.03.043.
781 Darzacq, X., Shav-Tal, Y., de Turris, V., Brody, Y., Shenoy, S.M., Phair, R.D., and Singer, R.H.
782 (2007). In vivo dynamics of RNA polymerase II transcription. Nat Struct Mol Biol *14*, 796-806.
783 10.1038/nsmb1280.
784 Dillon, M.T., Bergerhoff, K.F., Pedersen, M., Whittock, H., Crespo-Rodriguez, E., Patin, E.C.,
785 Pearson, A., Smith, H.G., Paget, J.T.E., Patel, R.R., et al. (2019). ATR Inhibition Potentiates the
786 Radiation-induced Inflammatory Tumor Microenvironment. Clin Cancer Res *25*, 3392-3403.
787 10.1158/1078-0432.CCR-18-1821.
788 Feng, X., Tubbs, A., Zhang, C., Tang, M., Sridharan, S., Wang, C., Jiang, D., Su, D., Zhang, H.,
789 Chen, Z., et al. (2020). ATR inhibition potentiates ionizing radiation-induced interferon response
790 via cytosolic nucleic acid-sensing pathways. EMBO J *39*, e104036. 10.15252/embj.2019104036.
791 Ferraro, P., Franzolin, E., Pontarin, G., Reichard, P., and Bianchi, V. (2010). Quantitation of
792 cellular deoxynucleoside triphosphates. Nucleic Acids Res *38*, e85. 10.1093/nar/gkp1141.
793 Foote, K.M., Nissink, J.W.M., McGuire, T., Turner, P., Guichard, S., Yates, J.W.T., Lau, A., Blades,
794 K., Heathcote, D., Odedra, R., et al. (2018). Discovery and Characterization of AZD6738, a Potent
795 Inhibitor of Ataxia Telangiectasia Mutated and Rad3 Related (ATR) Kinase with Application as an
796 Anticancer Agent. J Med Chem *61*, 9889-9907. 10.1021/acs.jmedchem.8b01187.
797 Ge, X.Q., Jackson, D.A., and Blow, J.J. (2007). Dormant origins licensed by excess Mcm2-7 are
798 required for human cells to survive replicative stress. Genes & development *21*, 3331-3341.
799 10.1101/gad.457807.

800 Ginno, P.A., Lott, P.L., Christensen, H.C., Korf, I., and Chedin, F. (2012). R-loop formation is a
801 distinctive characteristic of unmethylated human CpG island promoters. Mol Cell *45*, 814-825.
802 10.1016/j.molcel.2012.01.017.
803 Hall, A.B., Newsome, D., Wang, Y., Boucher, D.M., Eustace, B., Gu, Y., Hare, B., Johnson, M.A.,
804 Milton, S., Murphy, C.E., et al. (2014). Potentiation of tumor responses to DNA damaging
805 therapy by the selective ATR inhibitor VX-970. Oncotarget *5*, 5674-5685.
806 10.18632/oncotarget.2158.
807 Halliwell, J.A., Frith, T.J.R., Laing, O., Price, C.J., Bower, O.J., Stavish, D., Gokhale, P.J., Hewitt, Z.,
808 El-Khamisy, S.F., Barbaric, I., and Andrews, P.W. (2020). Nucleosides Rescue Replication-
809 Mediated Genome Instability of Human Pluripotent Stem Cells. Stem Cell Reports *14*, 1009-
810 1017. 10.1016/j.stemcr.2020.04.004.
811 Hazra, S., Szewczak, A., Ort, S., Konrad, M., and Lavie, A. (2011). Post-translational
812 phosphorylation of serine 74 of human deoxycytidine kinase favors the enzyme adopting the
813 open conformation making it competent for nucleoside binding and release. Biochemistry *50*,
814 2870-2880. 10.1021/bi2001032.
815 Hiraga, S.I., Ly, T., Garzon, J., Horejsi, Z., Ohkubo, Y.N., Endo, A., Obuse, C., Boulton, S.J.,
816 Lamond, A.I., and Donaldson, A.D. (2017). Human RIF1 and protein phosphatase 1 stimulate
817 DNA replication origin licensing but suppress origin activation. EMBO reports *18*, 403-419.
818 10.15252/embr.201641983.
819 Hoffmann, I., Draetta, G., and Karsenti, E. (1994). Activation of the phosphatase activity of
820 human cdc25A by a cdk2-cyclin E dependent phosphorylation at the G1/S transition. EMBO J
821 *13*, 4302-4310.
822 Hustedt, N., Alvarez-Quilon, A., McEwan, A., Yuan, J.Y., Cho, T., Koob, L., Hart, T., and Durocher,
823 D. (2019). A consensus set of genetic vulnerabilities to ATR inhibition. Open Biol *9*, 190156.
824 10.1098/rsob.190156.
825 Khan, M., and Gasser, S. (2016). Generating Primary Fibroblast Cultures from Mouse Ear and
826 Tail Tissues. J Vis Exp. 10.3791/53565.
827 Koppenhafer, S.L., Goss, K.L., Terry, W.W., and Gordon, D.J. (2020). Inhibition of the ATR-CHK1
828 Pathway in Ewing Sarcoma Cells Causes DNA Damage and Apoptosis via the CDK2-Mediated
829 Degradation of RRM2. Mol Cancer Res *18*, 91-104. 10.1158/1541-7786.MCR-19-0585.
830 Krebs, M.G., Lopez, J., El-Khoueiry, A.B., Bang, Y.-J., Postel-Vinay, S., Abida, W., Carter, L., Xu,
831 W., Im, S.-A., Pierce, A., et al. (2018). Abstract CT026: Phase I study of AZD6738, an inhibitor of
832 ataxia telangiectasia Rad3-related (ATR), in combination with olaparib or durvalumab in
833 patients (pts) with advanced solid cancers. Cancer research *78* (*Supplement*).
834 https://doi.org/10.1158/1538-7445.AM2018-CT026.
835 Kuskovsky, R., Buj, R., Xu, P., Hofbauer, S., Doan, M.T., Jiang, H., Bostwick, A., Mesaros, C., Aird,
836 K.M., and Snyder, N.W. (2019). Simultaneous isotope dilution quantification and metabolic
837 tracing of deoxyribonucleotides by liquid chromatography high resolution mass spectrometry.
838 Anal Biochem *568*, 65-72. 10.1016/j.ab.2018.12.023.
839 Kwok, M., Davies, N., Agathanggelou, A., Smith, E., Oldreive, C., Petermann, E., Stewart, G.,
840 Brown, J., Lau, A., Pratt, G., et al. (2016). ATR inhibition induces synthetic lethality and
841 overcomes chemoresistance in TP53- or ATM-defective chronic lymphocytic leukemia cells.
842 Blood *127*, 582-595. 10.1182/blood-2015-05-644872.

843   Langmead, B., and Salzberg, S.L. (2012). Fast gapped-read alignment with Bowtie 2. Nat
844   Methods *9*, 357-359. 10.1038/nmeth.1923.
845   Le, T.M., Poddar, S., Capri, J.R., Abt, E.R., Kim, W., Wei, L., Uong, N.T., Cheng, C.M., Braas, D.,
846   Nikanjam, M., et al. (2017). ATR inhibition facilitates targeting of leukemia dependence on
847   convergent nucleotide biosynthetic pathways. Nat Commun *8*, 241. 10.1038/s41467-017-
848   00221-3.
849   Liu, Q., Guntuku, S., Cui, X.S., Matsuoka, S., Cortez, D., Tamai, K., Luo, G., Carattini-Rivera, S.,
850   DeMayo, F., Bradley, A., et al. (2000). Chk1 is an essential kinase that is regulated by Atr and
851   required for the G(2)/M DNA damage checkpoint. Genes & development *14*, 1448-1459.
852   Lob, D., Lengert, N., Chagin, V.O., Reinhart, M., Casas-Delucchi, C.S., Cardoso, M.C., and Drossel,
853   B. (2016). 3D replicon distributions arise from stochastic initiation and domino-like DNA
854   replication progression. Nat Commun *7*, 11207. 10.1038/ncomms11207.
855   Mahbubani, H.M., Chong, J.P., Chevalier, S., Thommes, P., and Blow, J.J. (1997). Cell cycle
856   regulation of the replication licensing system: involvement of a Cdk-dependent inhibitor. J Cell
857   Biol *136*, 125-135.
858   Mailand, N., Falck, J., Lukas, C., Syljuasen, R.G., Welcker, M., Bartek, J., and Lukas, J. (2000).
859   Rapid destruction of human Cdc25A in response to DNA damage. Science *288*, 1425-1429.
860   10.1126/science.288.5470.1425.
861   Marchal, C., Sasaki, T., Vera, D., Wilson, K., Sima, J., Rivera-Mulia, J.C., Trevilla-Garcia, C.,
862   Nogues, C., Nafie, E., and Gilbert, D.M. (2018). Genome-wide analysis of replication timing by
863   next-generation sequencing with E/L Repli-seq. Nat Protoc *13*, 819-839.
864   10.1038/nprot.2017.148.
865   Mohni, K.N., Thompson, P.S., Luzwick, J.W., Glick, G.G., Pendleton, C.S., Lehmann, B.D.,
866   Pietenpol, J.A., and Cortez, D. (2015). A Synthetic Lethal Screen Identifies DNA Repair Pathways
867   that Sensitize Cancer Cells to Combined ATR Inhibition and Cisplatin Treatments. PLoS One *10*,
868   e0125482. 10.1371/journal.pone.0125482.
869   Moiseeva, T., Hood, B., Schamus, S., O'Connor, M.J., Conrads, T.P., and Bakkenist, C.J. (2017).
870   ATR kinase inhibition induces unscheduled origin firing through a Cdc7-dependent association
871   between GINS and And-1. Nat Commun *8*, 1392. 10.1038/s41467-017-01401-x.
872   Moiseeva, T.N., Qian, C., Sugitani, N., Osmanbeyoglu, H.U., and Bakkenist, C.J. (2019a). WEE1
873   kinase inhibitor AZD1775 induces CDK1 kinase-dependent origin firing in unperturbed G1- and
874   S-phase cells. Proc Natl Acad Sci U S A *116*, 23891-23893. 10.1073/pnas.1915108116.
875   Moiseeva, T.N., Yin, Y., Calderon, M.J., Qian, C., Schamus-Haynes, S., Sugitani, N.,
876   Osmanbeyoglu, H.U., Rothenberg, E., Watkins, S.C., and Bakkenist, C.J. (2019b). An ATR and
877   CHK1 kinase signaling mechanism that limits origin firing during unperturbed DNA replication.
878   Proc Natl Acad Sci U S A *116*, 13374-13383. 10.1073/pnas.1903418116.
879   O'Connor, M.J. (2015). Targeting the DNA Damage Response in Cancer. Mol Cell *60*, 547-560.
880   10.1016/j.molcel.2015.10.040.
881   Petryk, N., Kahli, M., d'Aubenton-Carafa, Y., Jaszczyszyn, Y., Shen, Y., Silvain, M., Thermes, C.,
882   Chen, C.L., and Hyrien, O. (2016). Replication landscape of the human genome. Nat Commun *7*,
883   10208. 10.1038/ncomms10208.
884   Robinson, J.T., Thorvaldsdottir, H., Winckler, W., Guttman, M., Lander, E.S., Getz, G., and
885   Mesirov, J.P. (2011). Integrative genomics viewer. Nat Biotechnol *29*, 24-26. 10.1038/nbt.1754.

886 Roulston, A., Zimmermann, M., Papp, R., Skeldon, A., Pellerin, C., Dumas-Berube, E., Dumais, V.,
887 Dorich, S., Fader, L.D., Fournier, S., et al. (2021). RP-3500: A Novel, Potent and Selective ATR
888 Inhibitor that is Effective in Preclinical Models as a Monotherapy and in Combination with PARP
889 Inhibitors. Mol Cancer Ther. 10.1158/1535-7163.MCT-21-0615.
890 Sanchez, Y., Wong, C., Thoma, R.S., Richman, R., Wu, Z., Piwnica-Worms, H., and Elledge, S.J.
891 (1997). Conservation of the Chk1 checkpoint pathway in mammals: linkage of DNA damage to
892 Cdk regulation through Cdc25. Science *277*, 1497-1501. 10.1126/science.277.5331.1497.
893 Sato, H., Niimi, A., Yasuhara, T., Permata, T.B.M., Hagiwara, Y., Isono, M., Nuryadi, E., Sekine, R.,
894 Oike, T., Kakoti, S., et al. (2017). DNA double-strand break repair pathway regulates PD-L1
895 expression in cancer cells. Nat Commun *8*, 1751. 10.1038/s41467-017-01883-9.
896 Sheu, Y.J., Kinney, J.B., and Stillman, B. (2016). Concerted activities of Mcm4, Sld3, and Dbf4 in
897 control of origin activation and DNA replication fork progression. Genome research *26*, 315-
898 330. 10.1101/gr.195248.115.
899 Sorensen, C.S., Syljuasen, R.G., Lukas, J., and Bartek, J. (2004). ATR, Claspin and the Rad9-Rad1-
900 Hus1 complex regulate Chk1 and Cdc25A in the absence of DNA damage. Cell Cycle *3*, 941-945.
901 Sukackaite, R., Cornacchia, D., Jensen, M.R., Mas, P.J., Blackledge, M., Enervald, E., Duan, G.,
902 Auchynnikava, T., Kohn, M., Hart, D.J., and Buonomo, S.B.C. (2017). Mouse Rif1 is a regulatory
903 subunit of protein phosphatase 1 (PP1). Sci Rep *7*, 2119. 10.1038/s41598-017-01910-1.
904 Tan, J.T., Dudl, E., LeRoy, E., Murray, R., Sprent, J., Weinberg, K.I., and Surh, C.D. (2001). IL-7 is
905 critical for homeostatic proliferation and survival of naive T cells. Proc Natl Acad Sci U S A *98*,
906 8732-8737. 10.1073/pnas.161126098.
907 Vendetti, F.P., Karukonda, P., Clump, D.A., Teo, T., Lalonde, R., Nugent, K., Ballew, M., Kiesel,
908 B.F., Beumer, J.H., Sarkar, S.N., et al. (2018). ATR kinase inhibitor AZD6738 potentiates CD8+ T
909 cell-dependent antitumor activity following radiation. J Clin Invest *128*, 3926-3940.
910 10.1172/JCI96519.
911 Vendetti, F.P., Lau, A., Schamus, S., Conrads, T.P., O'Connor, M.J., and Bakkenist, C.J. (2015).
912 The orally active and bioavailable ATR kinase inhibitor AZD6738 potentiates the anti-tumor
913 effects of cisplatin to resolve ATM-deficient non-small cell lung cancer in vivo. Oncotarget *6*,
914 44289-44305. 10.18632/oncotarget.6247.
915 Wang, C., Wang, G., Feng, X., Shepherd, P., Zhang, J., Tang, M., Chen, Z., Srivastava, M.,
916 McLaughlin, M.E., Navone, N.M., et al. (2019). Genome-wide CRISPR screens reveal synthetic
917 lethality of RNASEH2 deficiency and ATR inhibition. Oncogene *38*, 2451-2463. 10.1038/s41388-
918 018-0606-4.
919 Wengner, A.M., Siemeister, G., Lucking, U., Lefranc, J., Wortmann, L., Lienau, P., Bader, B.,
920 Bomer, U., Moosmayer, D., Eberspacher, U., et al. (2020). The Novel ATR Inhibitor BAY 1895344
921 Is Efficacious as Monotherapy and Combined with DNA Damage-Inducing or Repair-
922 Compromising Therapies in Preclinical Cancer Models. Mol Cancer Ther *19*, 26-38.
923 10.1158/1535-7163.MCT-19-0019.
924 Yoon, H., Kim, T.S., and Braciale, T.J. (2010). The cell cycle time of CD8+ T cells responding in
925 vivo is controlled by the type of antigenic stimulus. PLoS One *5*, e15423.
926 10.1371/journal.pone.0015423.
927 Zou, L., and Elledge, S.J. (2003). Sensing DNA damage through ATRIP recognition of RPA-ssDNA
928 complexes. Science *300*, 1542-1548. 10.1126/science.1083430.
929

Figures

Figure 1: ATRi selectively induces death in proliferating CD8$^+$ T cells *ex vivo*.

A. Proliferation of Pmel-1 CD8$^+$ T cells activated with gp100 *ex vivo*. CTV histograms of live, CD44^{hi} CD8$^+$ T cells at indicated time post-activation are shown. The number of cell divisions is shown. Red histograms are unactivated CD8$^+$ T cells. **B.** Immunoblots of CD8$^+$ T whole cell extracts prepared at 0 and 30 h post-activation. **C.** CD8$^+$ T cells were activated and treated with 5 µM AZD6738 (ATRi) from 0 - 24 h (blue) or 24 - 48 h (red). At 48 h, the percentage of live CD8$^+$ T cells (eFluor 780$^-$CD8$^+$TCRβ$^+$) was quantitated. **D.** Naïve CD8$^+$ T cells were maintained in IL-7 *ex vivo* (unactivated) and treated with 5 µM ATRi from 0 - 24 h or 24 - 48 h. At 48 h, the percentage of live CD8$^+$ T cells was quantitated. **E.** Exponentially diving B16 cells or primary fibroblasts were treated with ATRi for 24 h the percentage of live cells was quantitated. **F.** CD8$^+$ T cells were activated and treated with 5 µM ATRi, 500 nM ATMi (AZD0156), 5 µM PARPi (Olaparib), or 500 nM WEE1i (AZD1775) from 24 - 48 h. At 48 h, the percentage of live CD8$^+$ T cells was quantitated. **C-F.** Mean and SD bars shown. *:P < 0.05; **: P < 0.01; ***: P <0.001, ****: P <0.0001 by ANOVA with Tukey's multiple comparisons.

Figure 2: ATRi selectively induces death in proliferating CD8$^+$ T cells *in vivo*.

A-H. Immunoprofiling of tissues harvested on day 4 from CT26 tumor-bearing mice treated with 75 mg/kg AZD6738 (ATRi) or vehicle (Veh) on days 1-3. **A.** Quantitation of tumor-infiltrating (TIL) CD8$^+$ T cells (per mg of tumor) and quantitation of spleen and tumor-draining lymph node (DLN) CD8$^+$ T cells (as a percentage of total CD45$^+$ cells). **B.** Representative contour plots of Ki67$^+$ expression in CD8$^+$ T cells in the TIL, spleen, and DLN. **C.** Quantitation of proliferating (Ki67$^+$) CD8$^+$ T cells in the TIL, spleen, and DLN. **D.** Quantitation of CD69$^+$ CD8$^+$ T cells in the TIL, spleen, and DLN. **E.** Representative contour plots of KLRG1 and CD127 expression on CD62L^{lo} CD8$^+$ T cells in the TIL. **F.** Quantitation of KLRG1$^+$CD127$^-$ CD62L^{lo} CD8$^+$ T cells (as a percentage of total CD8$^+$ T cells) in the TIL. **G.** Representative contour plots of KLRG1 and CD69 expression on CD62L^{lo} CD8$^+$ T cells in the TIL. **H.** Quantitation of KLRG1$^+$CD69$^-$ CD62L^{lo} CD8$^+$ T cells (as a percentage of total CD8$^+$ T cells) in the TIL. **A-D.** n = 7 mice total (6 DLN for ATRi) from 2 independent experiments, each with 3-4 mice per arm. **E-H.** n = 4 (Veh) or 5 (ATRi) mice from one experiment. **A, C-D, F-H.**

960   Mean and SD bars shown. *:P < 0.05, **: P < 0.01, ***: P < 0.001, ****: P<0.0001 by two-tailed,

961   unpaired t-test.

962

963   **Figure 3: ATR kinase limits origin firing across active replicons in proliferating CD8$^+$ T cells.**

964   **A.** EdU versus DNA histograms of proliferating CD8$^+$ T cells and exponentially diving primary

965   fibroblasts. The percentage of cells in each cell cycle phase and the doubling time was used to

966   estimate the length of G1, S, and G2/M. **B.** Cartoon of the lengths of cell cycle and each phases

967   of proliferating CD8$^+$ T cells, B16 cancer cells, and primary fibroblasts drawn to scale. **C.**

968   Immunoblot of MCM4 in nuclease insoluble fraction in proliferating CD8$^+$ T cells treated with 5

969   µM ATRi, 500 nM ATMi (AZD0156), 5 µM PARPi (AZD2281/Olaparib), or 500 nM Wee1i (AZD1775)

970   for 1 h. **D.** Repli-seq analyses of the replication timing program of proliferating CD8$^+$ T cells

971   treated with DMSO (blue) or 5 µM AZD6738 (red) for 1 h. Upper – whole genome. Lower -

972   chromosome 1. Sequencing data are deposited at GEO (code: GSE183412). **E.** EdU incorporation

973   in early (2-3N) and late (3-4N) S phase in proliferating CD8$^+$ T cells treated with DMSO or 5 µM

974   ATRi for 1h. 10 µM EdU was added from 30-60 min. **F.** DNA fiber analyses of proliferating CD8$^+$ T

975   cells, B16, and primary fibroblasts treated with DMSO or 5 µM ATRi for 1 h. Cells were treated

976   with IdU from 30-40 min and CldU from 40-60 min of the treatment. **G.** Immunoblots of MCM4

977   in nuclease insoluble fraction in proliferating CD8$^+$ T cells treated with increasing concentrations

978   of Ro-3306 (CDK1i), CVT-313 (CDK2i), or PHA-767491 (CDC7i) for 75 min. Cells were treated with

979   ATRi from 15-75 min. **H.** Immunoblot of RIF1 phosphoserine-2153 (S2205 in human) in whole cell

980   extracts of proliferating CD8$^+$ T cells treated with increasing concentrations of Ro-3306 for 75 min.

981   Cells were treated with ATRi from 15-75 min. **I.** Immunoblot of MCM4 in the nuclease insoluble

982   fraction of proliferating CD8$^+$ T cells or B16 treated with 5 µM ATRi and/or 5 mM HU in the

983   sequence indicated. **J.** Model showing that ATR limits origin firing across active replicons. Green

984   circles indicate origins that fired and red circles indicate origins that have not fired. **E-F.** Mean

985   and SD bars shown. *: P < 0.05, **: P < 0.01, ***: P <0.001, ****: P <0.0001 by two-tailed,

986   unpaired t-test.

987   **Figure 4: Nucleosides rescue proliferating CD8$^+$ T cells from ATRi-induced cell death.**

988 **A.** Proliferating CD8$^+$ T cells were treated with nucleoside cocktails at 22 h and ATRi at 24 h . For

989 x2, proliferating CD8$^+$ T cells were treated with nucleoside cocktails at 22 h and 30 h. At 48 h, the

990 percentage of live CD8$^+$ T cells (eFluor 780$^-$CD8$^+$TCRβ$^+$) was quantitated. Low rN is 250 nM A, C,

991 G, and T. High rN is 15 µM A, C, G, and 6 µM T. EmbryoMax is 15 µM A, C, G, U, and 6 µM T. **B.**

992 CTV histograms of live (eFluor 780$^-$CD44^{hi}CD8$^+$) cells at 24 h (grey) or 48 h (blue) treated with

993 nucleosides and ATRi as described in panel A. Number of cell divisions is indicated. **C.** Immunoblot

994 of MCM4 in nuclease insoluble fraction in proliferating CD8$^+$ T cells treated low rN or high rN for

995 2 h prior to 5 µM ATRi for 1 h. Immunoblots of CHK1, CHK1 phosphoserine-345, and GAPDH are

996 from the soluble fraction. **D.** DNA combing analyses of proliferating CD8$^+$ T cells treated with high

997 rN for 2 h prior to 5 µM ATRi for 1 h. Cells were treated with IdU for from 30-40 min and CldU

998 from 40-60 min during the treatment with ATRi. **A and D (right panel).** Mean and SD bars shown.

999 *: P < 0.05, **: P < 0.01, ***: P <0.001, ****: P <0.0001 by one-way ANOVA with Tukey's multiple

1000 comparisons. **D (left panel).** *: P < 0.05, **: P < 0.01, ***: P <0.001, ****: P <0.0001 by two-

1001 tailed, unpaired t-test.

1002

1003 **Figure 5: Thymidine rescues proliferating CD8$^+$ T cells from ATRi-induced cell death.**

1004 **A.** Proliferating CD8$^+$ T cells were treated with either 15 µM A, C, G, or 6 µM T, or high rN at 22 h

1005 and ATRi at 24 h. At 48 h, the percentage of live CD8$^+$ T cells (eFluor 780$^-$CD8$^+$TCRβ$^+$) was

1006 quantitated. **B.** CTV histograms of live (eFluor 780$^-$CD44^{hi}CD8$^+$) cells at 24 h (grey) or 48 h (color)

1007 treated with nucleoside(s) and ATRi as described in panel A. Number of cell divisions is indicated.

1008 **C.** Proliferating CD8$^+$ T cells were treated with 6 µM T at 22 h and either ATRi or HU at 24 h. At

1009 30 h, cells were replated with and without 6 µM T. CTV histograms of live (eFluor 780$^-$CD44^{hi}CD8$^+$)

1010 cells at 24 h (grey), and 30 h and 48 h (with recovery) for ATRi- and HU-treated (6 h) samples

1011 (DMSO treated histograms in black; thymidine treated histograms in pink). Number of cell

1012 divisions is indicated. **D.** Proliferating CD8$^+$ T cells were activated and treated with 6 µM T at 22

1013 h and either ATRi or HU at 24 h. At 33 h, cells were replated with and without 6 µM T. At 48 h,

1014 the percentage of live CD8$^+$ T cells (eFluor 780$^-$CD8$^+$TCRβ$^+$) was quantitated. **A and D.** Mean and

1015 SD bars shown. *: P < 0.05, **: P < 0.01, ***: P <0.001, ****: P <0.0001 by one-way ANOVA with

1016 Tukey's multiple comparisons.

1017

1018 **Figure 6: ATRi induces degradation of RRM2 and DCK in proliferating CD8$^+$ T cells.**

1019 **A.** Quantitation of celluler deoxyribonucleosides in proliferating CD8$^+$ T cells treated with DMSO,

1020 5 µM ATRi, or 5 mM HU. **B.** Cartoon of nucleoside metabolism. **C-F.** Immunoblots of proliferating

1021 CD8$^+$ T whole cell extracts. **C.** Proliferating CD8$^+$ T cells were treated with 5 µM ATRi and 5 mM

1022 HU for 1 or 4 h. **D.** Proliferating CD8$^+$ T cells were treated with 5 µM MG132 (protease inhibitor)

1023 and 5 µM Ro-3306 (CDK1i) for 15 min prior to ATRi for 2 h. **E.** Proliferating CD8$^+$ T cells were

1024 treated with increasing concentrations of Ro-3306 (CDK1i) for 15 min followed by 5 µM ATRi for

1025 1 h. **F.** Proliferating CD8$^+$ T cells were treated with increasing concentrations of CVT-313 (CDK2i)

1026 for 15 min followed by 5 µM ATRi for 1 h. **G-H.** Whole cell extracts werre genrated from

1027 proliferating CD8$^+$ T cells treated with 5 µM ATRi and 5 µM CDK1i for 1 h. **G.** Proteins

1028 immunopurified with anti-pSPXK antibodies (phospho-MAPK/CDK substrates) were

1029 immunoblotted for RRM2. **H.** Proteins immunopurified with an anti-pSQ antibody (phospho-

1030 ATM/ATR substrates) were immunoblotted for DCK. **A.** Mean and SD bars shown. *: P < 0.05, **:

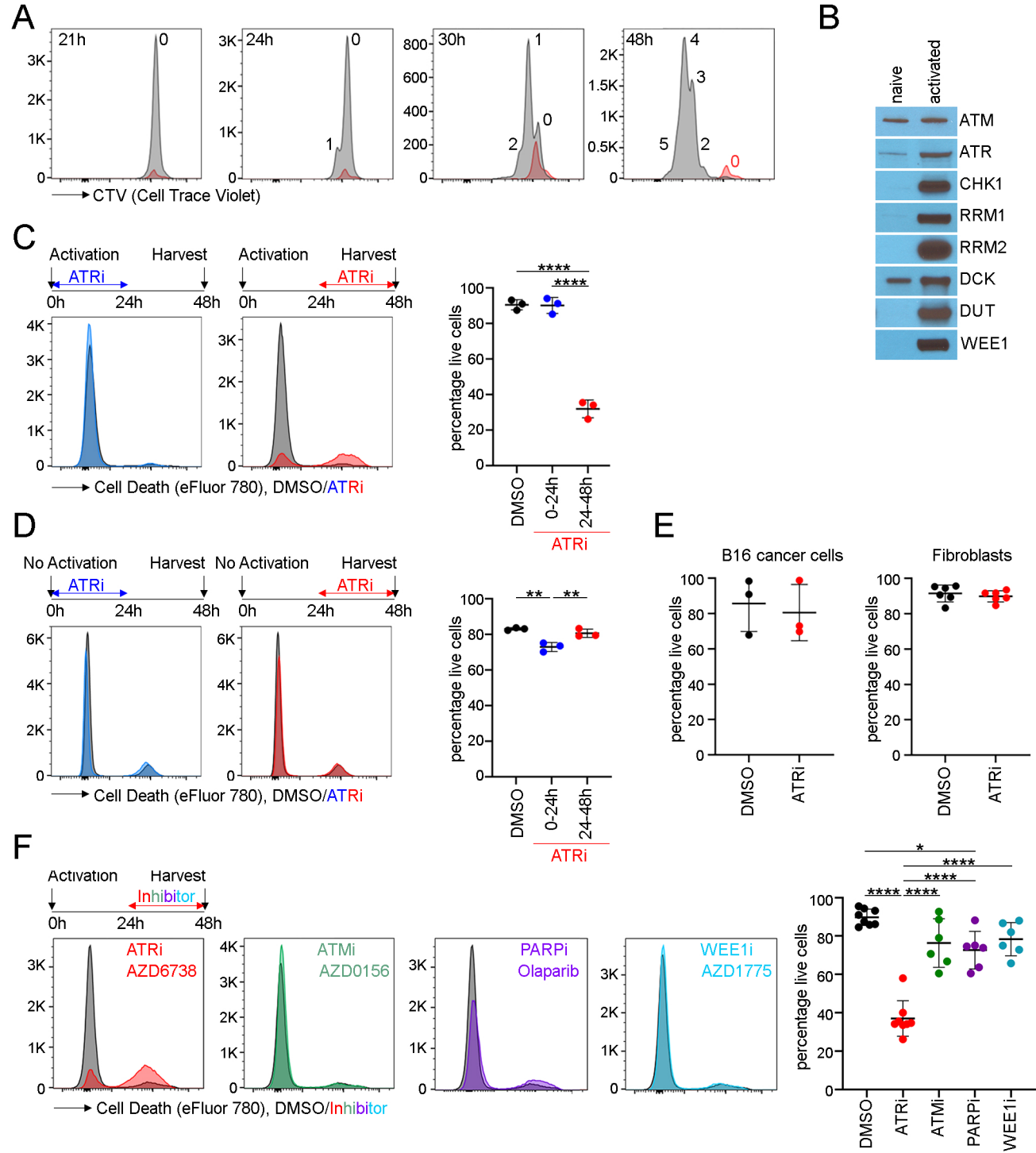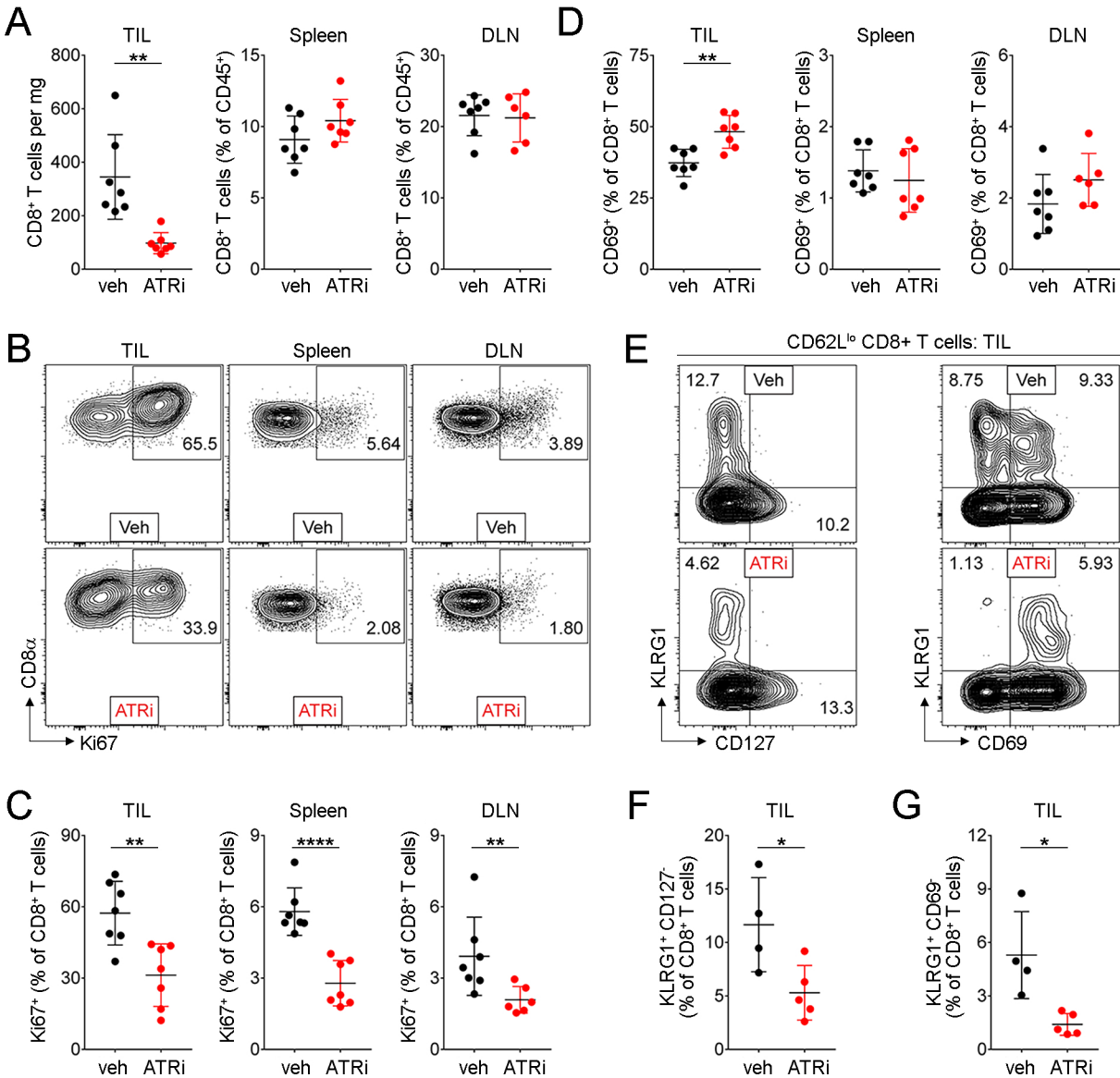1031 P < 0.01, ***: P <0.001, ****: P <0.0001 by one-way ANOVA with Dunnett multiple comparisons.

1032

1033 **Figure 7: ATRi-induces genome instabilty in proliferating CD8$^+$ T cells.**
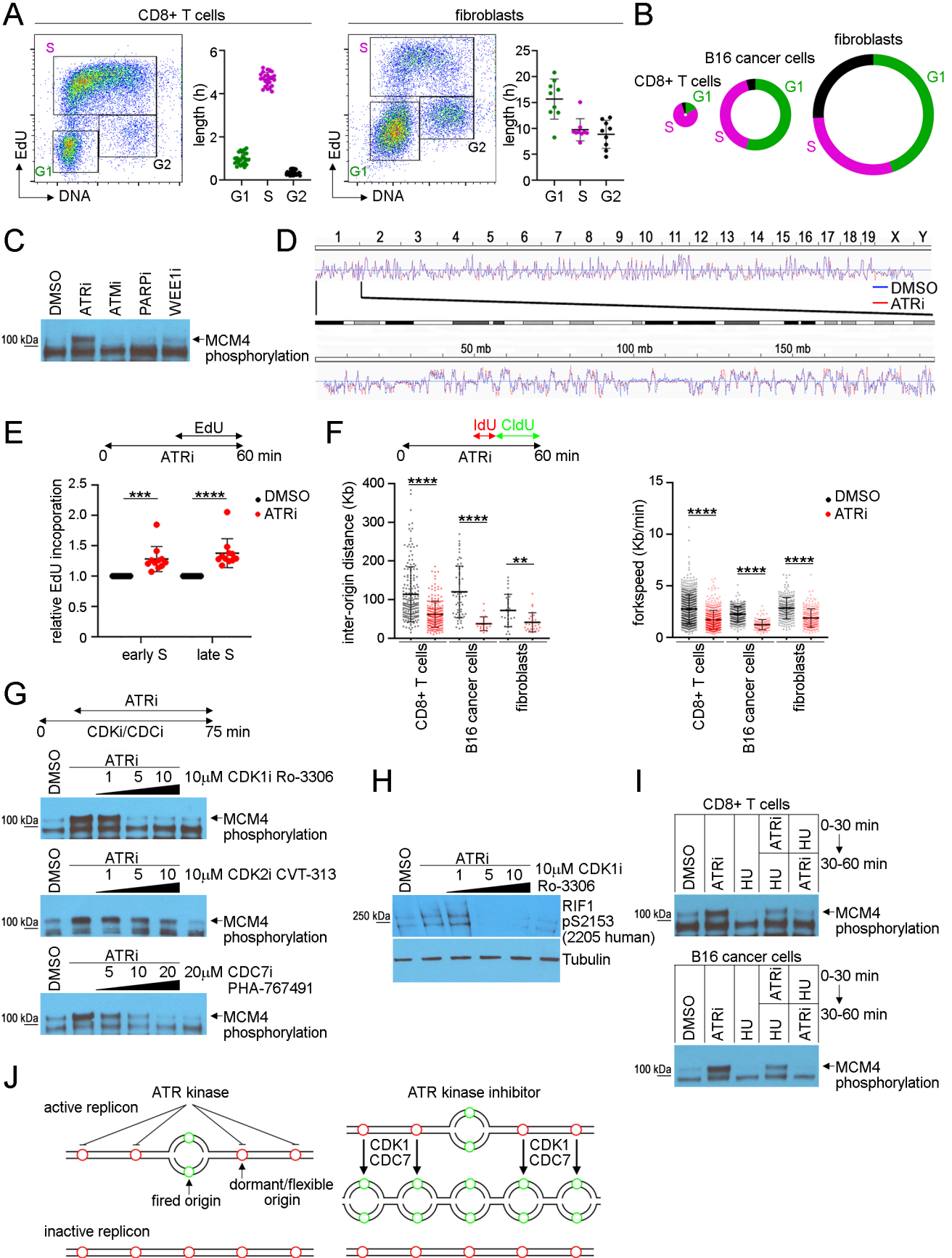
1034 **A.** Quantitation of dU contamination in genomic DNA prepared from proliferating CD8$^+$ T cells

1035 treated with 5 µM ATRi or 5 mM HU for 1 h. **B.** Quantitation of ɣH2AX in proliferating CD8$^+$ T cells

1036 treated with 6 µM thymidine for 2 h followed by 5 µM ATRi for 2 h or 4 h (upper). ɣH2AX versus

1037 DNA plots of proliferating CD8$^+$ T cells treated with 6 µM thymidine for 2 h followed by 5 µM ATRi

1038 for 2 h (lower). **C.** B16 and proliferating CD8$^+$ T cells were treated with 10 µM camptothecin

1039 (TOP1i) or 5 µM ATRi for 1 h. Genomic DNA was prepared and digested with restriction

1040 endonucleases, +/-RNASE H. DNA fragments were immunopurified with anti-RNA-DNA hybrid

1041 antibody (S9.6). Immunopuified DNA was dentured and and dot blotted using an anti-single-

1042 stranded DNA antibody. **D.** Representative images from the PLA of Pol II phosphoserine 5 and

1043 PCNA in proliferating CD8$^+$ T cells treated with 5 µM ATRi for 30 min. 10 µM EdU was added

1044 during the last 15 min of treatment. **E.** Quantitation of PLA described in panel D. **F.** Cartoon

1045 summarizing the mechanisms through wich ATRi induces genome instability in CD8$^+$ T cells. **A-B,**
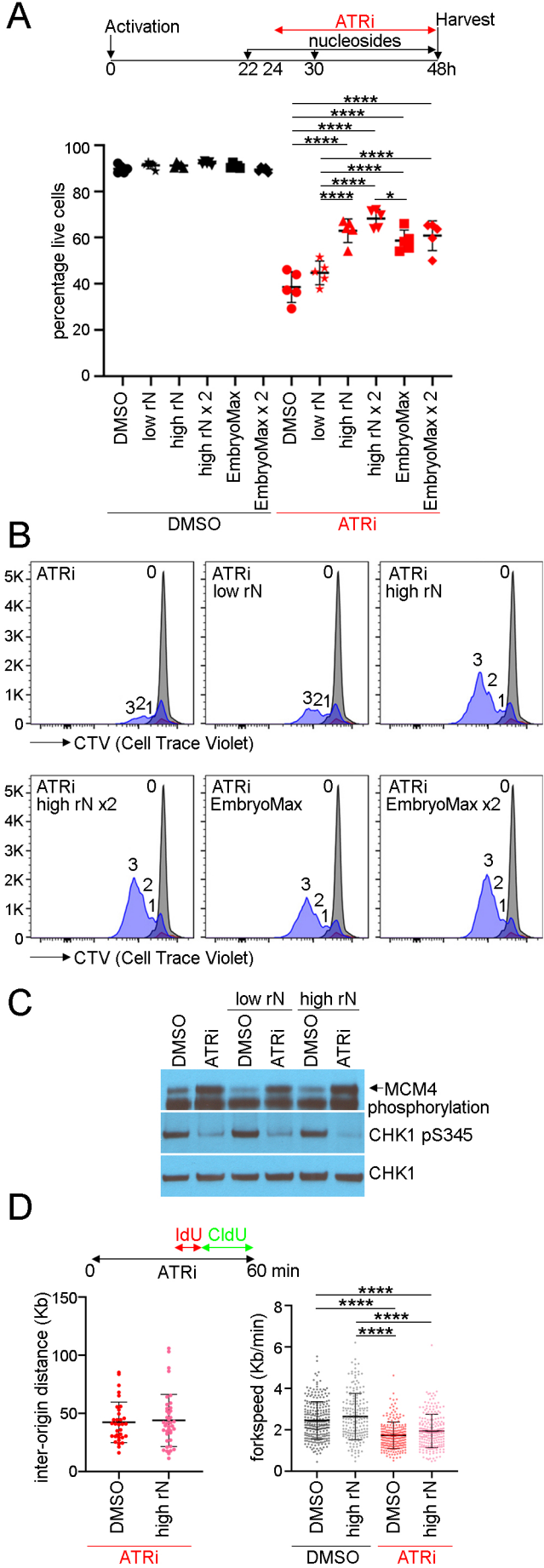
1046 **E.** Mean and SD bars shown. **A.** *: $P < 0.05$, **: $P < 0.01$, ***: $P < 0.001$, ****: $P < 0.0001$ by one-

1047 way ANOVA with Dunnett multiple comparisons. **B and E.** *: $P < 0.05$, **: $P < 0.01$, ***: $P < 0.001$,

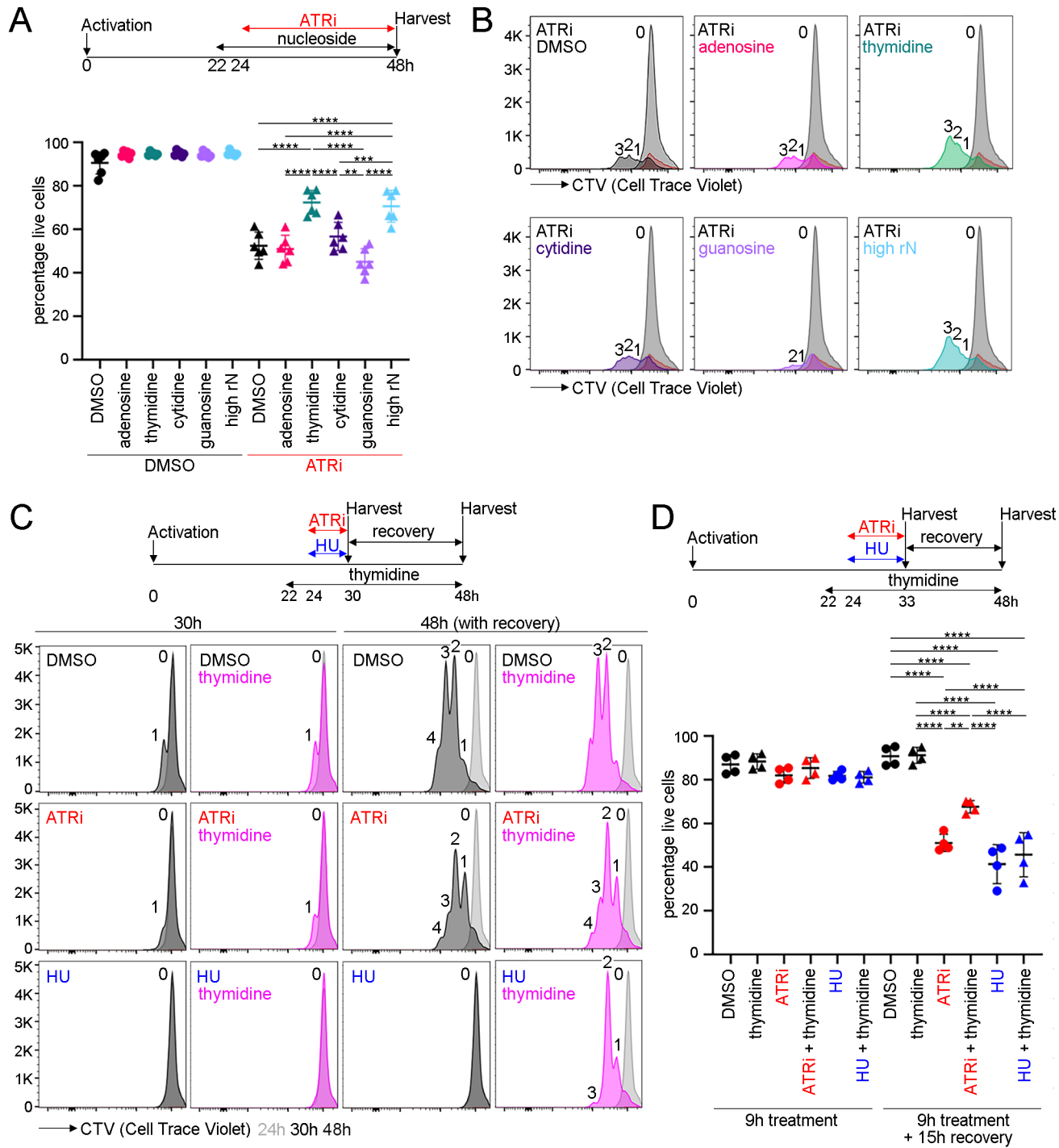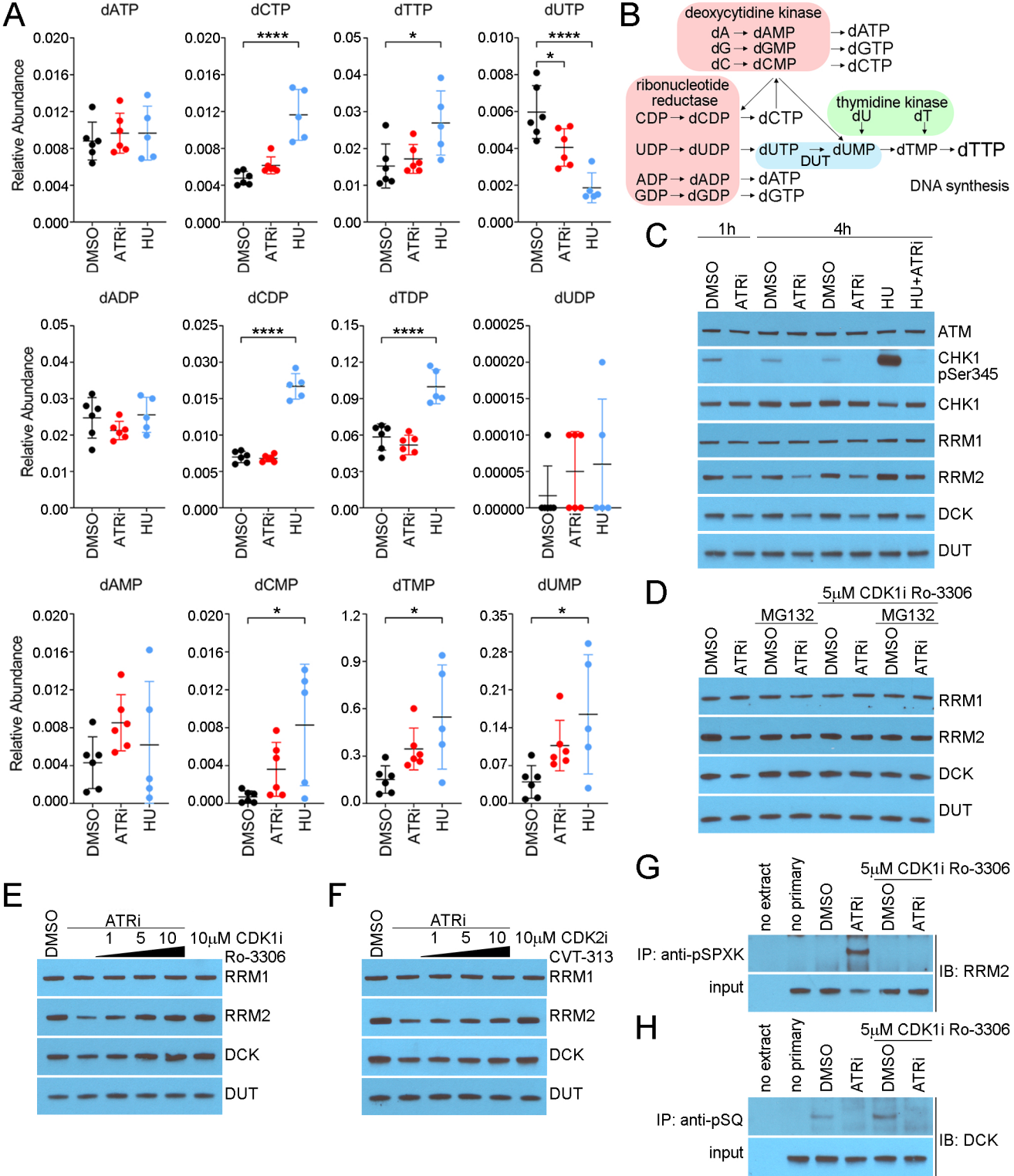1048 ****: $P < 0.0001$ by one-way ANOVA with Tukey's multiple comparisons.

1049

Sugitani et al. Figure 1

Sugitani et al. Figure 2

Sugitani et al. Figure 3

Sugitani et al. Figure 4

Sugitani et al. Figure 5

Sugitani et al. Figure 6
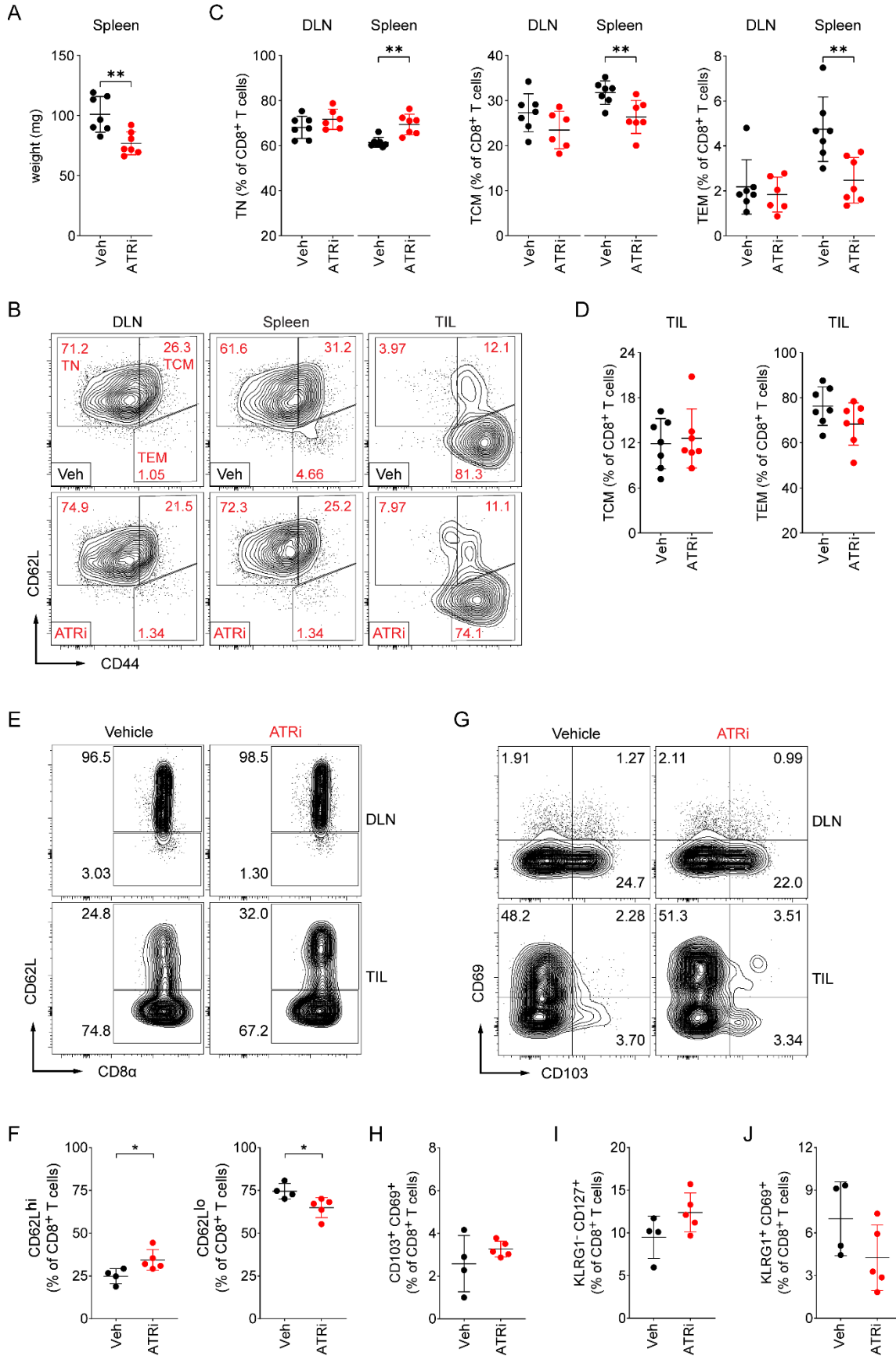
Sugitani et al Figure 7

Figure S1: A. Weight of whole spleens harvested on day 4 from CT26 tumor bearing mice treated with ATRi (75 mg/kg AZD6738) or vehicle (Veh) on days 1-3. **B-J.** Immunoprofiling of tissues harvested on day 4 from CT26 tumor bearing mice treated with ATRi (75 mg/kg AZD6738) or vehicle (Veh) on days 1-3. **B.** Representative contour plots of CD8$^+$ T cells with naïve (TN, CD62L^{hi}CD44^{lo}), central memory (TCM, CD62L^{hi}CD44^{hi}), and effector/effector memory (TEM, CD62L^{lo}CD44^{hi}) phenotypes in the tumor-draining lymph node (DLN), spleen, and tumor infiltrate (TIL). **C.** Quantitation of TN, TCM, and TEM CD8$^+$ T cells in the DLN and spleen. **D.** Quantitation of TCM and TEM CD8$^+$ T cells in the TIL. **E.** Representative contour plots of CD62L expression on CD8$^+$ T cells in the tumor-draining lymph node (DLN) and tumor infiltrate (TIL). **F.** Quantitation of CD62L^{hi} and CD62L^{lo} CD8$^+$ T cells in the TIL. **G.** Representative contour plots of CD69 and CD103 expression on CD8$^+$ T cells in the DLN and TIL. **H.** Quantitation of CD103$^+$CD69$^+$ (tissue resident) CD8$^+$ T cells in the TIL**. I.** Quantitation of KLRG1$^-$CD127$^+$ CD62L^{lo} (memory precursor effector) CD8$^+$ T cells (as a percentage of total CD8$^+$ T cells) in the TIL. **J.** Quantitation of KLRG1$^+$CD69$^+$ CD62L^{lo} CD8$^+$ T cells (as a percentage of total CD8$^+$ T cells) in the TIL. **A-D.** n = 7 mice total per group (6 DLN for ATRi) from 2 independent experiments, each with 3-4 mice per group. **E-J.** n = 4 (Veh) or 5 (ATRi) mice. **A, C-D, F, H-J.** Mean and SD bars shown. *: P < 0.05, **: P < 0.01 by two-tailed, unpaired t-test. Brackets not shown for comparisons that were not statistically significant.
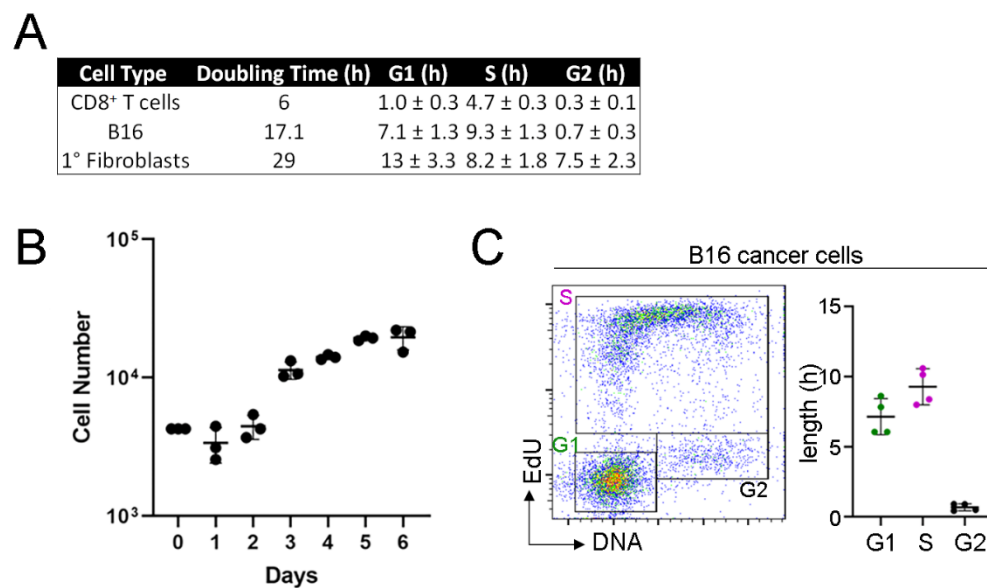
A

Cell Type	Doubling Time (h)	G1 (h)	S (h)	G2 (h)
CD8+ T cells	6	1.0 ± 0.3	4.7 ± 0.3	0.3 ± 0.1
B16	17.1	7.1 ± 1.3	9.3 ± 1.3	0.7 ± 0.3
1° Fibroblasts	29	13 ± 3.3	8.2 ± 1.8	7.5 ± 2.3

Figure S2: A. Summary of doubling times and estimated lengths of G1, S, and G2 phases in CD8+ T cells, B16, and primary fibroblasts. The percentage of cells in each cell cycle phase and the doubling time was used to estimate the length of G1, S, and G2/M. **B.** Doubling time of B16 was previously reported (Danciu et al., 2013; Fidler, 1975) while that of primary fibroblasts was calculated with the equation (t2 − t1)/(3.32*log(n2/n1)) using linear part of the growth curve. n1 is the cell number at the time point t1 and n1 is the cell number at the time point t2. **C.** EdU versus DNA histograms of B16. Mean and SD bars shown.

Danciu, C., Falamas, A., Dehelean, C., Soica, C., Radeke, H., Barbu-Tudoran, L., Bojin, F., Pinzaru, S.C., and Munteanu, M.F. (2013). A characterization of four B16 murine melanoma cell sublines molecular fingerprint and proliferation behavior. Cancer Cell Int *13*, 75. 10.1186/1475-2867-13-75.
Fidler, I.J. (1975). Biological behavior of malignant melanoma cells correlated to their survival in vivo. Cancer research *35*, 218-224.
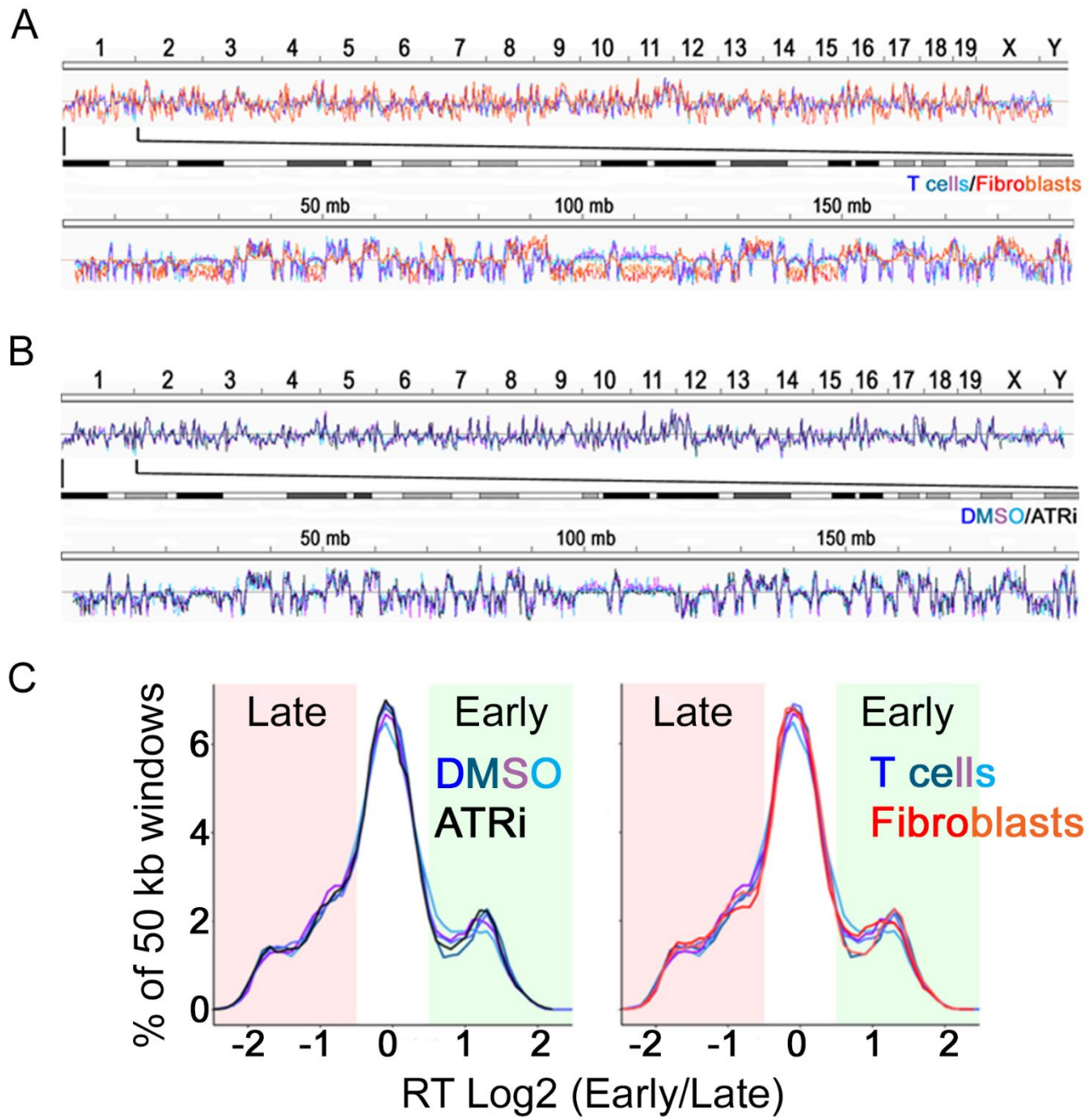
Figure S3: A. Repli-seq analyses of proliferating CD8^{+} T cells (blues) and primary fibroblasts (reds). Upper – whole genome. Lower - chromosome 1. Sequencing data are deposited at GEO (code: GSE183412). **B.** Repli-seq analyses of proliferating CD8^{+} T cells treated with DMSO (blues) or 5 µM AZD6738 (black) for 1 h. **C.** Genome-wide distribution of the replication timing of 50 kb genomic windows determined by repli-seq. Comparison of proliferating CD8^{+} T cells treated with DMSO (blues) or 5 µM AZD6738 (black) (left panel) or proliferating CD8^{+} T cells treated with DMSO (blues) and primary fibroblasts treated with DMSO (reds) (right panel).

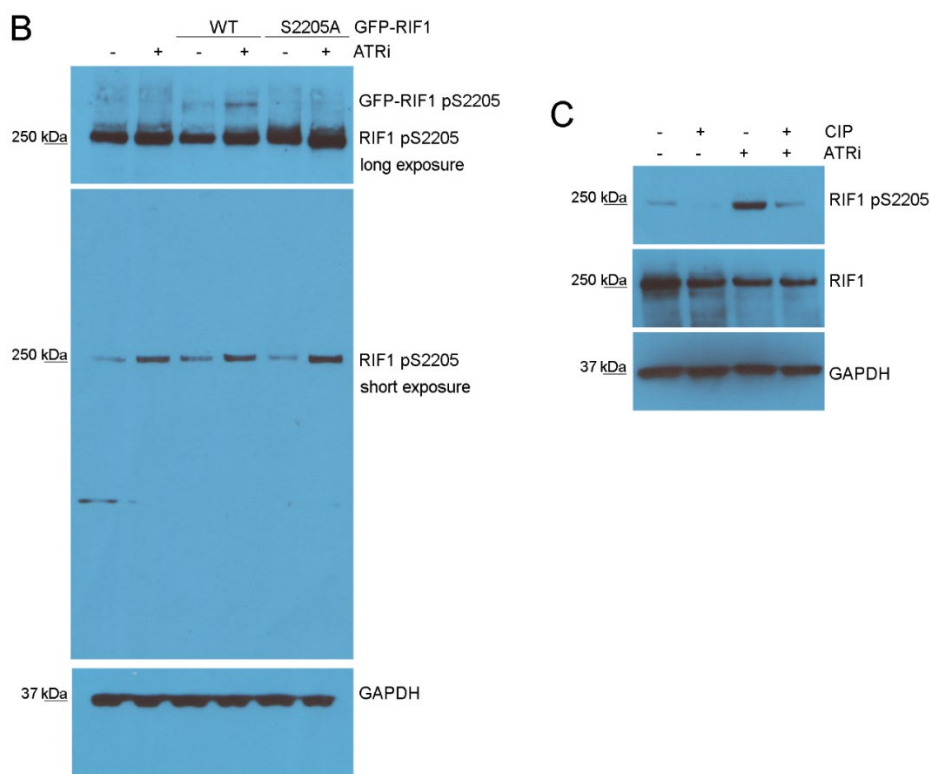| Concentration (ng/mL)	1,000.00	500.00	250.00	125.00	62.50	31.25	15.62	7.81	3.90	1.95	Blank		
Dilution	1:1,000	1:2,000	1:4,000	1:8,000	1:16,000	1:32,000	1:64,000	1:128,000	1:256,000	1:512,000	Blank	Titer	Coating
107C2-2	2.792	2.739	2.778	2.686	2.567	2.387	2.202	1.867	1.495	1.067	0.056	>1:512,000	A
107C2-2	0.054	0.057	0.060	0.055	0.052	0.057	0.066	0.052	0.055	0.058	0.057	<1:1,000	B

Figure S4: A. A rabbit monoclonal antibody was generated against a synthetic peptide CKVRRV(pSer)FADPI. ELISA of the hybridoma supernatant shows selectivity against phosphopeptide A: CKVRRV(pSer)FADPI vs. nonphosphopeptide B: CKVRRVSFADPI. **B.** GFP-RIF1 WT (wild-type) or GFP-RIF1 S2205A mutated were expressed in 293T cells. Cells were treated with ATRi for 1 h and whole cell extracts were generated and immunoblotted using the purified rabbit monoclonal antibody from A. Upper panel is a long exposure that shows that GFP-RIF1 WT, but not GFP-RIF1 S2205A mutated, is recognized by the rabbit monoclonal antibody in cells treated with ATRi. Middle panel is a typical exposure that shows that endogenous RIF1 is recognized by the rabbit monoclonal antibody in whole cell extracts of 293T cells treated with ATRi. **C.** Whole cell extracts of 293T cells treated with vehicle or ATRi were treated with calf intestinal phosphatase (CIP). RIF1 is recognized by the rabbit monoclonal antibody in whole cell extracts of 293T cells treated with ATRi and this is reversed by treatment with CIP.
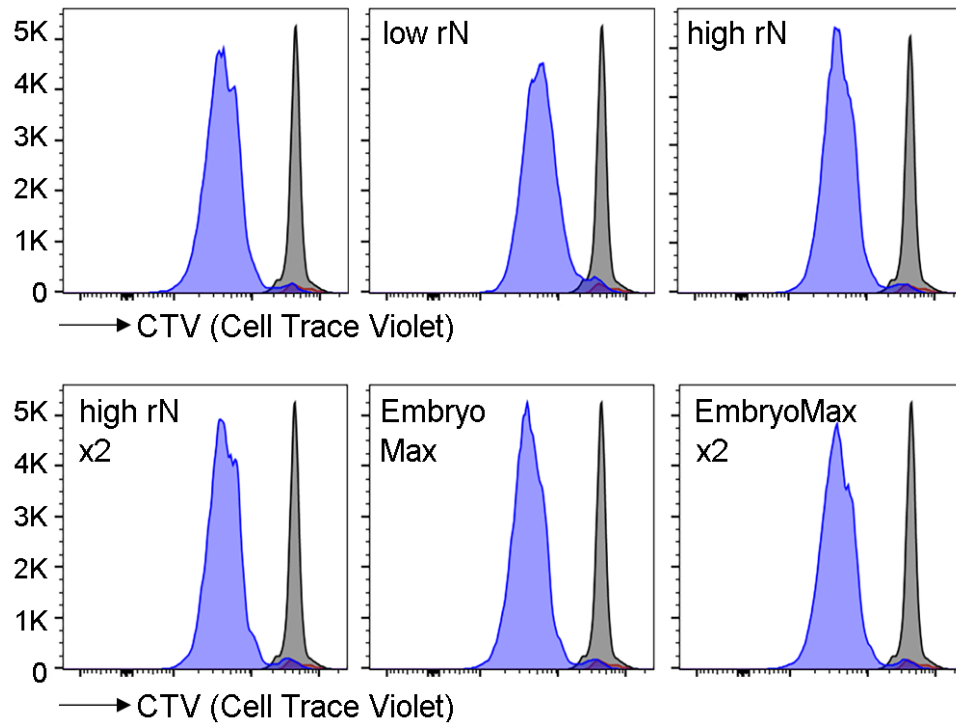
Figure S5:

Representative overlays of CTV (proliferation) histograms for proliferating CD8+ T cells treated with DMSO and different nucleosides analyzed at 24 h (gray) or 48 h (blue), corresponding to Figure 4A. Red histogram represent unactivated samples. CTV histograms are within live, CD44hiCD8+ gates.
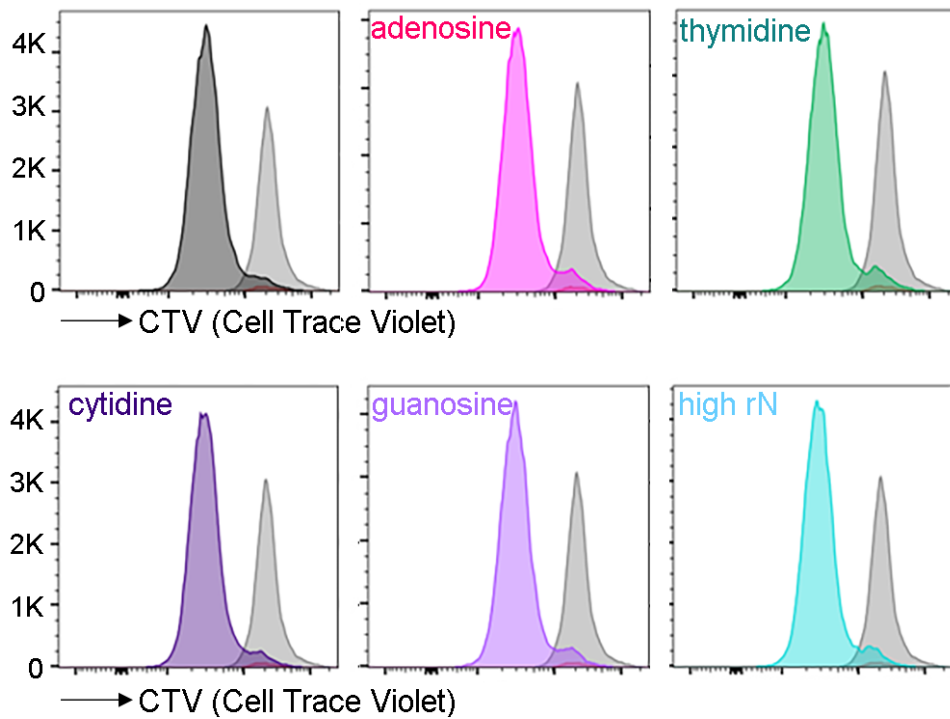
Figure S6: Representative overlays of CTV (proliferation) histograms for proliferating CD8+ T cells treated with DMSO and different nucleosides analyzed at 24 h (gray) or 48 h (blue), corresponding to Figure 5A. Red histogram represent unactivated samples. CTV histograms are within live, CD44hiCD8+ gates.
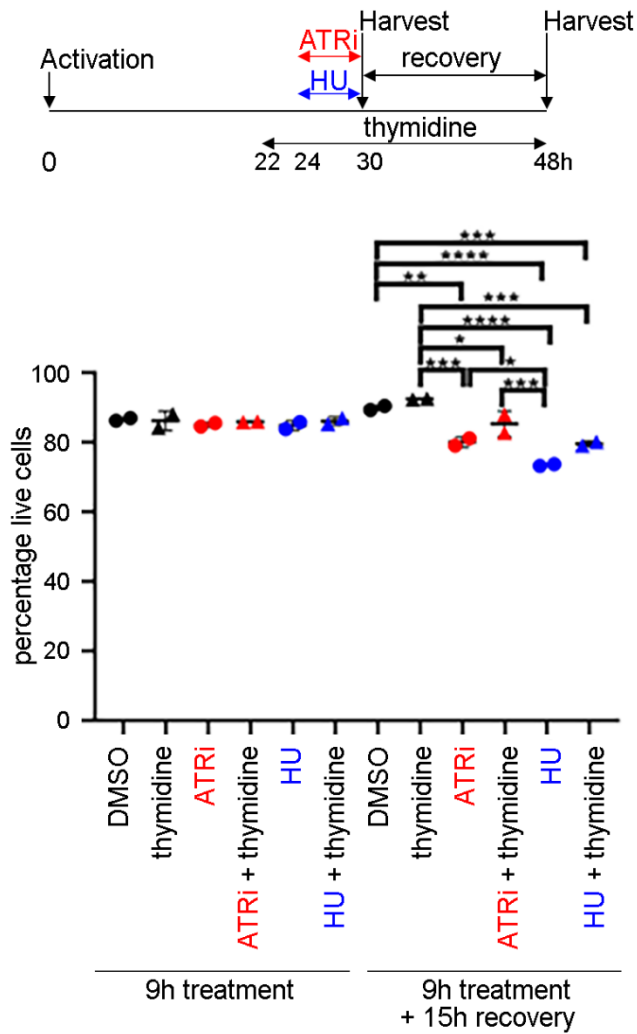
Figure S7: Percentage of live CD8+ T cells (eFluor 780-CD8+TCRβ+) was quantitated for the experiment described in Figure 5C. Mean and SD bars shown. Statistics represent one-way ANOVA with Tukey's multiple comparisons where *: $P < 0.05$, **: $P < 0.01$, ***: $P < 0.001$, ****: $P < 0.0001$. Brackets not shown for comparisons that were not statistically significant and between DMSO and ATRi treated samples for clarity.
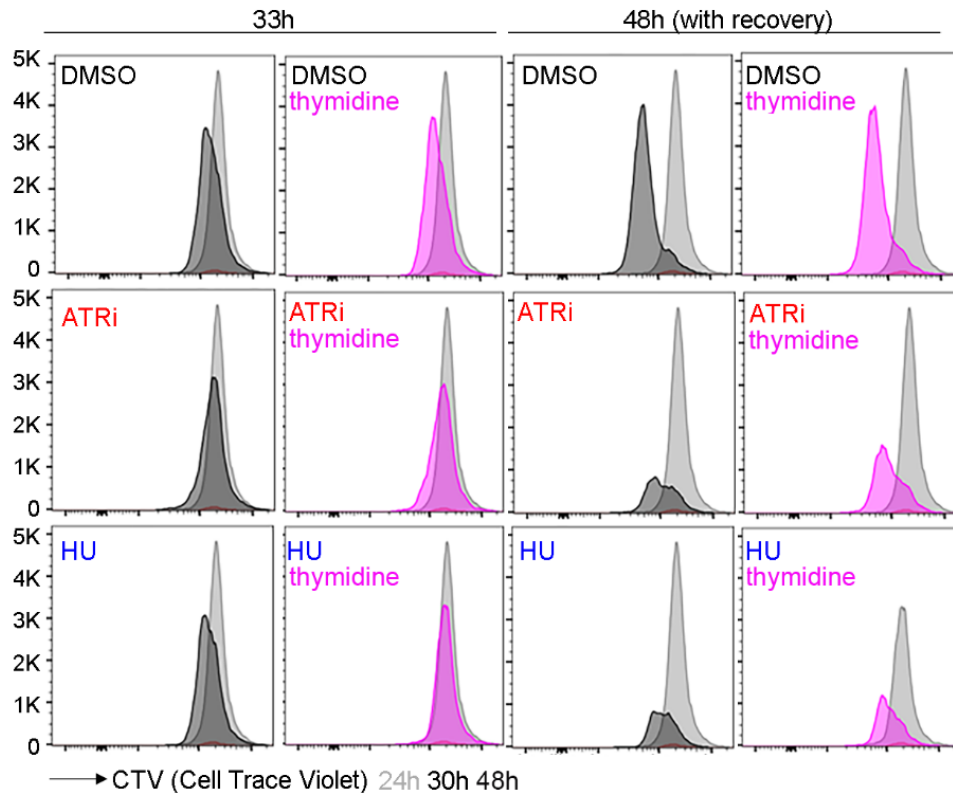
Figure S8: Representative overlays of CTV (proliferation) histograms at 24 h (gray), 33 h or 48 h post stimulation for proliferating CD8+ T cells treated with ATRi or HU and DMSO (black) or thymidine (pink) , corresponding to the experiemnt described in Figure 5D. CTV histograms are within live, CD44hiCD8+ gates.

SUPPLEMENTAL METHODS

Table SM1: Antibodies used in this work.

Antibody	Dilution	Manufacturer	Catalog #
CD8+ T cell activation			
Anti-mouse CD28		BD Biosciences	553294
Anti-mouse CD3Ɛ		BioLegend	100331
Proliferation/ survival assay			
AF647 anti-mouse CD44 (IM7)	1:500	BioLegend	103018
PE anti-mouse CD8α (53-6.7)	1:250	BioLegend	100708
AF488 anti-mouse TCR-β (H57-597)	1:250	BioLegend	10925
***In vivo* immunophenotyping**			
BV650 anti-mouse CD4 (clone GK1.5)	1:500	BD Biosciences	563232
BV786 anti-mouse CD62L (clone MEL-14)	1:1000	BD Biosciences	564109
AF488 anti-mouse TCR-β (H57-597)	1:250	BioLegend	109215
AF647 anti-mouse Ki67 (clone 16A8)	1:200	BioLegend	652408
BV421 anti-mouse CD69 (clone H1.2F3)	1:250	BioLegend	104545
BV510 anti-mouse CD4 (clone GK1.5)	1:500	BioLegend	100449
BV510 anti-mouse CD45 (clone 30-F11)	1:250	BioLegend	103138
BV650 anti-mouse CD127 (IL-7Rα) (clone A7R34)	1:100	BioLegend	135043
PE anti-mouse/human CD44 (clone IM7)	1:500	BioLegend	103007
PE anti mouse/human KLRG1 (MAFA) (clone 2F1/KLRG1)	1:250	BioLegend	138407
PE-Cy7 anti-mouse CD8α (clone 53-6.7)	1:250	BioLegend	100721
PerCP-Cy5.5 anti-mouse CD103 (clone 2E7)	1:50	BioLegend	121416
TruStain FcX PLUS anti-mouse CD16/32 (clone S17011E)	1:100	BioLegend	156604
AF647 anti-mouse CD8 (clone KT15)	1:500	MBL Intl	D271-A64
Western blot			
ATM (D2E2)	1:1000	Cell Signaling	2873
ATR	1:1000	Cell Signaling	2790
CHK1 (2G1D5)	1:1000	Cell Signaling	2360
Phospho-CHK1 (S345) (133D3)	1:1000	Cell Signaling	2348
RRM1	1:1000	Cell Signaling	3388
RRM2 (N1C1)	1:1000	GeneTex	GTX103193
DCK	1:1000	Abcam	ab96599
DUT	1:1000	LSBio	LS-C80791
WEE1 (D10D2)	1:1000	Cell Signaling	13084
MCM4 (D3H6N)	1:1000	Cell Signaling	12973
α-Tubulin	1:1000	Cell Signaling	2144
RIF1 pS2205 (CUSTOM)	1:5000	Genescript	107C2-2
ssDNA	1:1000	Millipore	MAB3034

DNA Combing				
IdU (BrdU)	1:20	BD Biosciences	347580
CldU (BrdU)	1:50	abcam	ab6326
ssDNA	1:50	Millipore	MAB3034
anti-mouse AF594	1:50	Invitrogen	A11005
anti-rat AF488	1:50	Invitrogen	A21470
anti-mouse AF647	1:50	Invitrogen	A21235
Immunoprecipitation				
Phospho-MAPK/CDK Substrates (PXS*P or S*PXR/K) (34B2)	1:50	Cell Signaling	2325
Phopho-ATM/ATR Substrate (S*Q) (D23H2/D69H5) MultiMab™	1:50	Cell Signaling	9607
S9.6		Millipore	MABE1095
PLA				
PCNA	1:5000	Abcam	ab92552
phospho-RNA polymerase II (S5)	1:100000	Abcam	ab5408
γH2AX flow cytometry				
FITC anti-mouse γH2AX	1:250	BioLegend	613404

Table SM2: Reagents used for the quantitation of free nucleotides by LC-HRMS.

| Reagent	Manufacturer	Catalog #
Optima LC-MS grade water	Thermo Fisher Scientific	W6-4
Optima LC-MS grade acetonitrile	Thermo Fisher Scientific	A955-4
Optima LC-MS grade methanol	Thermo Fisher Scientific	A456-4
1,1,1,3,3,3-hexafluoro 2-propanol (HFIP)	Sigma-Aldrich	105228
Diisopropylethylamine (DIPEA)	Sigma-Aldrich	D125806
AMP standard	Sigma-Aldrich	1930
dAMP standard	Sigma-Aldrich	D6375
ATP standard	Sigma-Aldrich	A26209
dATP standard	Sigma-Aldrich	D6500
dTMP standard	Sigma-Aldrich	T7004
dTTP standard	Sigma-Aldrich	T0251
CMP standard	Sigma-Aldrich	C1006
dCMP standard	Sigma-Aldrich	D7625
CTP standard	Sigma-Aldrich	C1506
dCTP standard	Sigma-Aldrich	D4635
UMP standard	Sigma-Aldrich	U6375
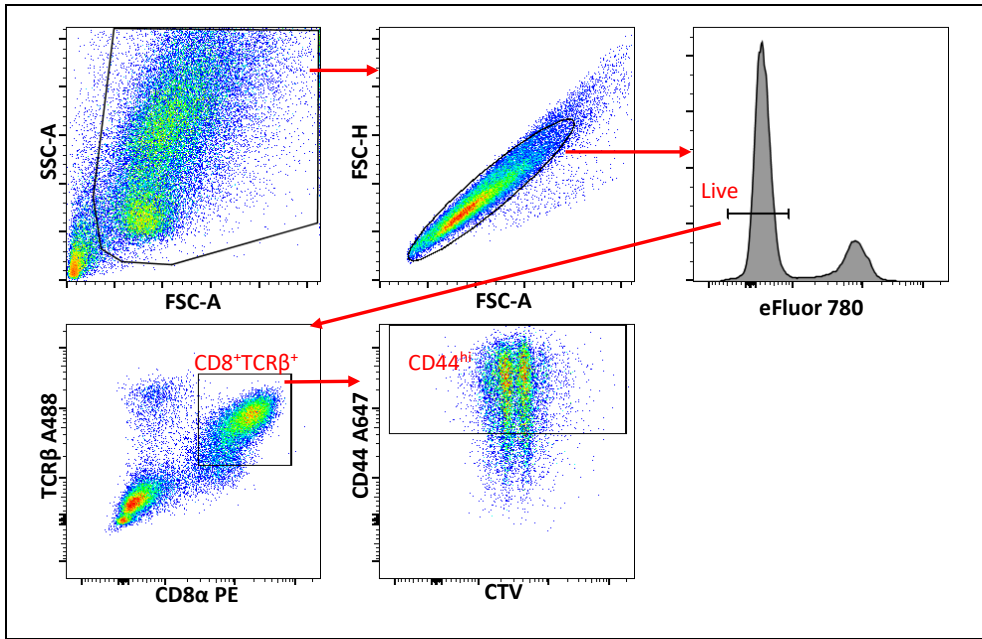
Figure SM1: Flow cytometry gating strategy for CD8+ T cells *ex vivo*.

Any unstable portions of the run were gated out prior to analysis. *Ex vivo* cultured CD8+ T cells were gated first with scatter gating (FSC-A vs. SSC-A) to exclude debris followed by single cell gating (FSC-A vs. FSC-H) to remove doublets/clumps. For proliferation assay, CD8+ T cells were identified as CD8+TCRβ+ cells within live population. CTV proliferation dye dilution was further characterized in CD44hi population within these cells.
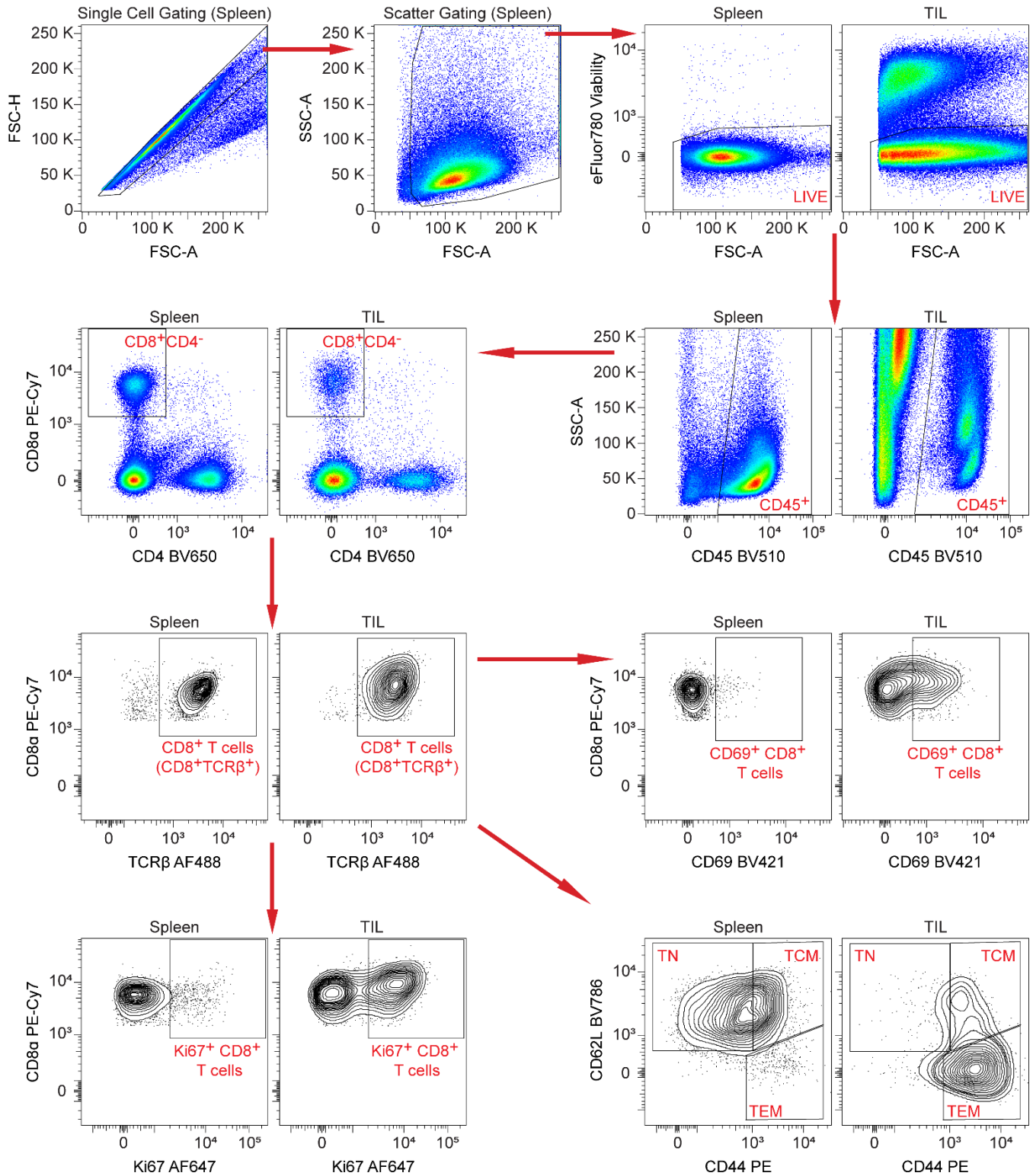
Supplemental Figure SM2.

Flow cytometry gating strategy for CD8$^+$ T cell profiling in spleen, TIL, and DLN. Any unstable portions of the run were gated out prior to analysis. After single cell gating (FSC-A vs. FSC-H) to remove doublets/clumps and scatter gating (FSC-A vs. SSC-A) to exclude debris, CD8$^+$ T cells were identified as CD8$^+$CD4$^-$TCRβ$^+$ cells within the live, CD45$^+$ immune cell population. CD8$^+$ T cells were further profiled to identify proliferating (Ki67$^+$), newly activated (CD69$^+$), naïve (TN, CD62L^{lo}CD44^{lo}), central memory (TCM, CD62L^{hi}CD44^{hi}), and effector/effector memory (CD62L^{lo}CD44^{hi}) CD8$^+$ T cells. Example plots are shown for spleen and TIL for all gating following single cell and scatter gating.
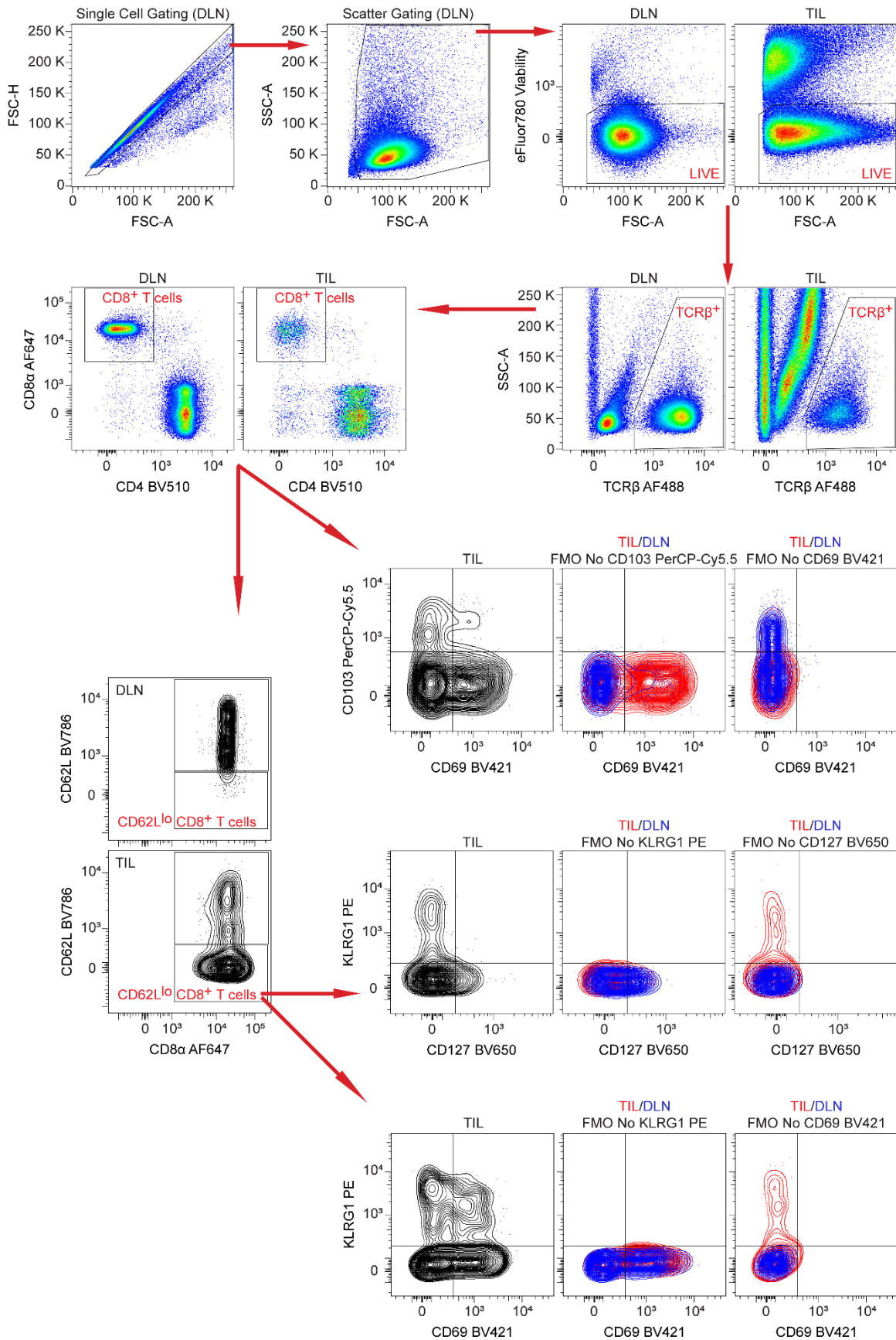
Supplemental Figure SM3.

Flow cytometry gating strategy for effector CD8$^+$ T cell profiling in TIL and DLN. Any unstable portions of the run were gated out prior to analysis. After single cell gating (FSC-A vs. FSC-H) to remove doublets/clumps and scatter gating (FSC-A vs. SSC-A) to exclude debris, CD8$^+$ T cells were identified as TCRβ$^+$CD8$^+$CD4$^-$ cells within the live cell population. Tissue resident CD8$^+$ T cells in the TIL were identified as CD103$^+$CD69$^+$. Expression of CD62L was examined on CD8$^+$ T cells in the TIL and DLN, and the CD62L^{lo} CD8$^+$ T cell population (which includes effector/effector memory CD8$^+$ T cells) in the TIL was further profiled for expression of KLRG1, CD127, and CD69 to identify short-lived/terminal effector (KLRG1$^+$CD127$^-$), memory precursor effector (KLRG1$^-$CD127$^+$), newly activated KLRG1$^+$ effector (KLRG1$^+$CD69$^+$), and previously activated KLRG1$^+$ effector (KLRG1$^+$CD69$^-$) CD8$^+$ T cells. Example plots are shown for DLN and TIL for all gating following single cell and scatter gating, and for TIL following gating of CD62L^{lo} CD8+ T cells. Both TIL and DLN fluorescence minus one (FMO) controls were used to empirically determine gating for KLRG1, CD127, and CD69, and are shown as overlaid plots (TIL in red, DLN in blue).